

UNIVERSITAT POLITÈCNICA DE CATALUNYA

BACHELOR'S THESIS IN ENGINEERING PHYSICS

---

**Implementation of a Bayesian algorithm  
into Mantid for the analysis of neutron  
scattering data to reveal molecular  
movements**

---

*Author:*

Diego Monserrat López

*Supervisor:*

Dr. Luis Carlos Pardo Soto

Group of Characterization of Materials

Barcelona

January 2016



# *Abstract*

Data fitting and model selection lie at the very heart of the scientific method, however, these tasks are often tackled via the use of popular (and typically unquestioned) optimization algorithms of limited validity or flexibility. To circumvent these limitations, this work introduces an adaptive Markov chain Monte Carlo method for, through Bayesian Inference, performing fitting of experimental data. This method allows to obtain  $\chi^2$  probability density functions without assuming any frequentist supposition, and taking into account correlation between fitting parameters by direct exploration of the parameter space.

This work mainly consists in the creation of a powerful fitting tool based on the aforementioned robust inference method. In fact, it is presented the implementation of the algorithm FABADA (Fitting Algorithm for Bayesian Analysis of Data) within the *Man-tid* framework. The power of this algorithm is illustrated by revisiting an overarching and recurring question in the interpretation of quasielastic neutron scattering measurements, that is, how many spectral components may (or may not) be justified by the available experimental data.

Finally, an accurate Bayesian analysis is performed over real quasielastic neutron scattering measurements, in order to study the molecular reorientation dynamics of Cl-adamantane in its plastic phase. A calorimetric study [1] over this compound shows an anomalous heat-capacity behavior around  $T = 310$  K, which is inside the temperature range of the plastically crystalline phase. So, this work has the aim of prove if the molecular dynamics can be related with this phenomenon. The analysis performed shows how, since the consideration of Cl-adamantane such as an oblong shaped molecule, there is variation on the degree of anisotropy of the rotational diffusion approximately at the temperature of interest.



## *Acknowledgements*

First of all, I would like to express my gratitude to Dr. Luis Carlos Pardo, for giving me the opportunity to work with this project and for his dedication and guidance as supervisor of this bachelor's thesis. Secondly, I would like to thank the ISIS Molecular Spectroscopy Group, particularly Dr. Félix Fernández-Alonso and Dr. Sanghamitra Mukhopadhyay, for the great treatment and good advice all they gave me during my stays with the group. I am also grateful to my colleagues Roman Tolchenov, from the Mantid Development team, for his valuable guidance with the software development, and Alessandro Vispa, from the Group of Characterization of Materials, for his helpful contribution.

Finally, I would like to thank my family and friends, whose support has been invaluable throughout all these years at university.



# Contents

<b>Abstract</b>	<b>iii</b>
<b>Acknowledgements</b>	<b>v</b>
<b>1 Introduction</b>	<b>1</b>
<b>2 Bayesian inference</b>	<b>3</b>
2.1 The ubiquitous $\chi^2$ . . . . .	3
2.2 Adaptive Markov chain Monte Carlo method . . . . .	4
2.3 FABADA . . . . .	6
2.4 Model selection . . . . .	7
<b>3 Mantid Implementation</b>	<b>11</b>
3.1 Using FABADA within Mantid . . . . .	12
3.1.1 The visual interfaces . . . . .	12
3.1.2 A look to the results . . . . .	14
3.1.3 Writing a Python script . . . . .	17
3.2 Coclusions and prospects . . . . .	18
<b>4 How many lines are there?</b>	<b>21</b>
4.1 Data generation . . . . .	21
4.2 Model selection . . . . .	23
4.3 Conclusions . . . . .	24
<b>5 Neutron scattering overview</b>	<b>25</b>
5.1 Coherent and incoherent scattering . . . . .	25
5.2 Correlation functions . . . . .	27
5.3 IRIS instrument . . . . .	28
5.3.1 Principle of operation . . . . .	29
<b>6 The dynamics of Cl-Adamantane</b>	<b>31</b>
6.1 Chloroadamantane . . . . .	31
6.2 The QENS experiment . . . . .	32
6.3 Analysis and discussion . . . . .	33
6.4 Conclusions . . . . .	40
<b>Bibliography</b>	<b>41</b>



# Chapter 1

## Introduction

Data fitting is the standard way to ascertain how correctly a model describes experimental results and to obtain parameters that describe the underlying physics processes. It also allows to perform model selection by quantifying the success of a hypothesis to describe the experimental measurements. Despite being a crucial component of the scientific method, data fitting is not always tackled via the most appropriate way.

Frequentist methods, such as Levenberg-Marquardt algorithm (also known as the damped least-squared method), are the most popular when performing data fitting. These methods are based in the minimization of a cost function, usually  $\chi^2$  (defined in section 2.1). The goal is to obtain the set of parameters' values, with their associated errors, which best describes the experimental data ( $P_i \pm \epsilon_i$ ). Therefore, the minimum value for  $\chi^2$ , the associated to optimal values of the parameters, is used as figure of merit in order to quantify the fitting quality. In other words, the veracity of the hypothesis, which in this case is the mathematical model.

Frequentist approximation for data analysis has as the main drawback that it usually gets stuck in local minima of the  $\chi^2$  hypersurface when starting far away the global minimum or if the model is complex. In fact, frequentist methods involve certain suppositions that deserve to be considered. They suppose that there is only one minimum in the  $\chi^2\{P_i\}$  hypersurface and that the functional dependence of  $\chi^2\{P_i\}$  is quadratic on each parameter  $i$ , therefore only symmetric errors are allowed. Moreover, frequentist approach discards possible correlations between parameters.

In front of frequentist approximation we can find Bayesian inference, which does not need any supposition on the  $\chi^2\{P_i\}$  landscape [2]. A Bayesian analysis results in a different completely manner to express fitted parameters and the figure of merit showing all the complexity of the final solution: they become Probability Distribution Function (PDFs) obtained directly from exploring the  $\chi^2\{P_i\}$  hypersurface. Chapter 2 will focus on Bayesian inference as well as on a Markov chain Monte Carlo (MCMC) method, which is a way to achieve the desired PDFs. We also will introduce how to get this technique adaptive in order to optimize the parameter space exploration. Furthermore, we will see how Bayesian inference allows to perform model selection in a completely different way, full of benefits [3].

The main objective of the present thesis is, beyond explaining the intrinsic aspects of Bayesian analysis as well as showing its advantages with respect to frequentist methods, to convert it into a useful and powerful tool for the user. Therefore, the algorithm FABADA (Fitting Algorithm for Bayesian Analysis of Data) [4], based on the adaptive MCMC method, will be implemented into Mantid (chapter 3), which is a software for

neutron scattering data treatment and analysis. For doing that, it will be necessary to write all the code, right from the start, in order to perform the technique defined by the algorithm. It must be done accomplishing all Mantid software framework requirements, in order to get a full implementation. This means to get FABADA usable through the Mantid interface, but also to work taking advantage of all the possible internal software structures, functions and tools.

In chapter 4, the power of this new MANTID tool is illustrated by revisiting an overarching and recurring question in the interpretation of quasielastic neutron scattering measurements, that is, how many spectral components may (or may not) be justified by the available experimental data. The content of this study has allowed the author, along with his research fellows, to publish the scientific article *FABADA Goes MANTID to Answer an Old Question: How Many Lines Are There?* [5].

As it has been commented, Mantid is originally a software for neutron scattering data treatment and, in fact, neutron scattering will be the topic of the second part of the thesis. Chapter 5 will be a basic overview of neutron scattering fundamentals, aimed to understand the basic concepts that will be needed later. It will also be introduced IRIS instrument from the ISIS neutron source at Rutherford Appleton Laboratory, where it has been performed an experiment on Cl-Adamantane, which analysis will be the topic of chapter 6.

A calorimetric study over Cl-Adamantane shows an anomalous heat-capacity behaviour around  $T = 310$  K [1]. Otherwise, several studies [6, 7, 8] prove Cl-Adamantane presents an orientationally disordered phase, also called plastic phase, in certain temperature range including 310 K. Where, despite molecular centres of mass remain distributed along a lattice positions, molecules keep moving over themselves, but without total freedom. The aim of the experiment is to use neutron scattering to study the molecular dynamics of the Cl-Adamantane plastic phase, in order to discern a possible relation with the calorimetric effect observed. For that purpose, the resulting data will be tackled through an accurate Bayesian analysis.

# Chapter 2

## Bayesian inference

In this chapter we will go deeply into the Bayesian inference and will try to particularize, through adaptive Markov chain Monte Carlo, a method to perform data fitting. Finally, we will see how the results that Bayesian inference approach provides can be used to evaluate which hypothesis are more suitable to the data analysed [9].

### 2.1 The ubiquitous $\chi^2$

In order to quantify the quality of an experimental data fitting with a mathematical model it is defined the figure of merit  $\chi^2$ ,

$$\chi^2 = \sum_{k=1}^n \frac{(H_k\{P_i\} - D_k)^2}{\sigma_k^2} \quad (2.1)$$

where  $n$  is the number of experimental points,  $D_k (k = 1, \dots, n)$  are the experimental data,  $H_k\{P_i\} (k = 1, \dots, n)$  are the values obtained from the hypothesis (mathematical model) using the  $\{P_i\} (i = 1, \dots, m)$  set of parameters, being  $m$  the number of parameters, and  $\sigma_k (k = 1, \dots, n)$  are the experimental errors associated with the respective measured points  $D_k$ . Hence, data fitting is usually done by minimizing  $\chi^2$ , which aims to find the minimum of the  $\chi^2\{P_i\}$  hypersurface.

Another interesting figure of merit to introduce for the future is the reduced  $\chi^2$ ,

$$\chi_{red}^2 = \frac{\chi^2}{n - m - 1} \quad (2.2)$$

where  $n$  is the number of experimental points and  $m$  is the number of parameters, so  $n - m - 1$  is the number of degrees of freedom. Sometimes, when comparing different hypotheses with different number of parameters, it is reasonable to penalize the addition of parameters and  $\chi_{red}^2$  is defined for that.

The objective of Bayesian methods is to find the probability that a hypothesis is true given some experimental evidence, and they are based on the well-known Bayes theorem [10]:

$$P(H_k|D_k) = \frac{P(D_k|H_k)P(H_k)}{P(D_k)} \quad (2.3)$$

where  $P(H_k|D_k)$  is called the *posterior*, the probability that the hypothesis is in fact describing the data.  $P(D_k|H_k)$  is the *likelihood*, the probability that our data is well described by our hypothesis.  $P(H_k)$  is called the *prior*, the knowledge (as probability

density function) we have beforehand about the hypothesis, and  $P(D_k)$  is a normalization factor to assure that the integrated posterior probability is unity.

Here we are considering the case in which the experiment consists in a series of data  $D_k$  and the hypothesis is a mathematical model which depends on different parameters. Hence, the objective of the fitting is to find the values of these parameters which best adjust the mathematical model to experimental data. In the following, we will assume no prior knowledge (maximum ignorance *prior*), so Bayes theorem takes the simple form:

$$P(H_k|D_k) \propto P(D_k|H_k) \equiv L \quad (2.4)$$

where  $L$  is a short notation for likelihood.

In order to quantify Bayes theorem, we need to determine the likelihood that one single data point  $D_{k=i}$  is described by the hypothesis. In a counting experiment, this probability follows a Poisson Distribution but, when the number of counts is high enough, it can be approximated by a Gaussian distribution with  $\sigma = \sqrt{D_k}$ . Therefore, for one experimental point ( $k = i; i = 1, \dots, n$ ):

$$P(D_{k=i}|H_{k=i}) = \frac{H_k^{D_k} \cdot e^{-H_k}}{D_k!} \approx \frac{1}{\sigma\sqrt{2\pi}} \cdot e^{-\frac{1}{2}\left(\frac{H_k-D_k}{\sigma_k}\right)^2} \quad (2.5)$$

Hence, the likelihood that the full set of data  $D_k$  is described by the hypothesis  $H_k$  becomes:

$$P(D_k|H_k) \propto \prod_{k=1}^n e^{-\frac{1}{2}\left(\frac{H_k-D_k}{\sigma_k}\right)^2} = e^{-\frac{1}{2}\sum_{k=1}^n \left(\frac{H_k-D_k}{\sigma_k}\right)^2} = e^{-\frac{\chi^2}{2}} \quad (2.6)$$

Finally we get an expression to quantify the probability of the hypothesis validity, which depends on the  $\chi^2$ . This expression for the likelihood and the probabilistic understanding of  $\chi^2$  are going to be fundamental in the coming sampling method

## 2.2 Adaptive Markov chain Monte Carlo method

In statistics, Markov Chain Monte Carlo (MCMC) methods are a class of algorithms for constructing a Markov chain of a desired distribution by sampling a probability distribution. In the case that concern us, the probabilistic understanding of  $\chi^2$  makes it possible to define a unique method in order to explore the  $\chi^2$  hypersurface, first to fit the experimental data, and then to analyse the obtained results. This method is based in the Metropolis algorithm [11], but it introduces a tuning of the parameter change allowed, which becomes crucial for the success in finding the global  $\chi^2\{P_i\}$  minimum in an efficient way.

Algorithm starts with whatever values for hypothesis parameters, which usually are called first guess. Then, a new set of parameters values  $P^{new}$  are generated from an old set  $P^{old}$  by randomly changing just one of them:

$$P_i^{new} = P_i^{old} + (RND - 0.5) \cdot 2P_{jump}^i \quad (2.7)$$

where  $P_{jump}^i$  is called the parameter jump and  $RND$  is a gaussian random number, generated from a distribution centered at 0 and with a unity standard deviation.

The new cost function  $\chi^2$  value is calculated having into account the change on parameter  $i$ . In the case that  $\chi^2$  is lowered, the new set of parameter is automatically accepted. Nevertheless, the same way there is thermal agitation in classical Monte Carlo simulations, there are errors associated with the data. Therefore, there is a non-zero probability to accept new sets of parameters that increase the cost function  $\chi^2$  value. In our case, that probability is given by:

$$\frac{P(H_k(P_i^{new})|D_k)}{P(H_k(P_i^{old})|D_k)} = e^{-\frac{\chi_{new}^2 - \chi_{old}^2}{2}} \quad (2.8)$$

It is important to underline that these a priori illegal movements to higher values of  $\chi^2$  enable jumps over small barriers in the  $\chi^2$  landscape. This way of exploring the parameter space has some similarities with Gibbs sampling technique, something we will recall later for going deeper on its advantages.

In most frequentist approaches, such as Levenberg-Marquardt algorithm, the initialization of parameters is critical to the convergence of the algorithm. However, by the tuning of the parameter jump  $P_{jump}^i$  it is possible to get the sampling adaptive to the fitting parameters. Hence, it will be this jump what will decide the success of the algorithm to find the global  $\chi^2\{P_i\}$  minimum in an efficient way. If the parameter jumps are chosen too small, the algorithm will always accept any parameter change, getting lost in irrelevant details of the  $\chi^2\{P_i\}$  landscape. If chosen too large, the parameters will hardly be accepted, and the algorithm will get stuck every now and then. Therefore, in order to optimize the parameter space exploration, it is proposed the following adaptive MCMC scheme.

Given the number of algorithm steps  $N_i$  (number of iterations of eq. 2.7 for each parameter  $i$ ) and the number of steps  $K_i$  when new sets of parameter  $P_i^{new}$  have been accepted, it is defined the ratio  $R_i$  of steps for parameter  $i$  leading to a  $\chi^2$  changes as  $R_i = \frac{K_i}{N_i}$ . On the other hand,  $R_{i,desired}$  is the ratio with which parameter  $i$  should be accepted throughout the process. As we want every parameter to be changed with the same ratio we can define a single variable  $R_{desired}$  (i.e.  $R_{i,desired} = R_{desired} \quad \forall i = 1, \dots, m$ ). Hence, the updating of parameter jump  $P_{jump}^i$  is done every certain number of steps (regeneration time) following the expression:

$$\left[ P_{jump}^i \right]_{new} = \left[ P_{jump}^i \right]_{old} \cdot \frac{R_i}{R_{i,desired}} \quad (2.9)$$

where  $R_i$  is the acceptance ratio until the updating moment. Eq. 2.9 leads all parameters to have the same acceptance ratio and equal to  $R_{desired}$ . If during algorithm

iterations, changes of a parameter  $P_i$  are too often accepted, the parameter space is being overexplored with regard to parameter  $i$  and  $R_i > R_{desired}$ . Therefore eq. 2.9 makes the new  $P_{jump}^i$  larger in order to reduce its acceptance. Otherwise, if the acceptance is too low, the new  $P_{jump}^i$  becomes smaller.

In order to obtain a proper performance, it is needed to get the algorithm equally sensitive to all parameters changes. This fact is crucial, because when parameter jumps are not properly chosen, the parameter space can be overexplored in the direction of those parameters with too small jump lengths; in other words, the model would be insensitive to the proposed change of these parameters. Therefore, it is important to achieve the exploration of all of them equally efficient.

Finally, it is necessary to define a criteria in order to determine when a fitting parameter has already converged. The criteria introduced by eq. 2.10 says that parameter  $i$  have converged when its change, after an algorithm step, leads to a  $\chi^2$  relative decrease lower than a certain value (which will be called  $CC$  from *convergence criteria*):

$$\frac{\chi_{old}^2 - \chi_{new}^2}{\chi_{old}^2} < CC \quad (2.10)$$

### 2.3 FABADA

FABADA, the acronym for **F**itting **A**lgorithm for **B**ayesian **A**nalysis of **D**Ata, is an algorithm based on the adaptive MCMC technique and Bayesian inference explained previously [4]. The algorithm consists in two parts, one is the fitting process, from the beginning until all parameters have converged, and the other one is the generation of the full MCMC chain for a further analysis.

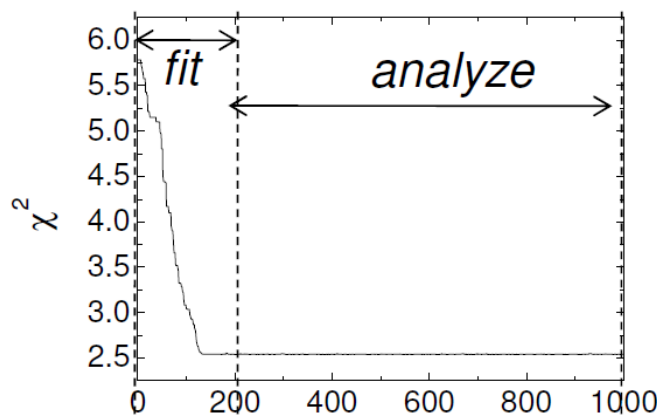


FIGURE 2.1: Plot of  $\chi^2$  values throughout a FABADA process, where it is distinguished the fitting part from the part corresponding to the chain generation for the analysis.

For generating the MCMC chain for the analysis, FABADA continues running the sampling defined by eq. 2.7 after all parameters have converged, until the number of steps desired by the user (this number could be typically between 1 and 10 million of steps). Actually, in order to avoid correlation between two consecutive sets of parameters and to reduce the amount of data to be proceeded without losing information, it is used a saving rate chosen by the user. Instead of saving the set of parameters for each step, only one out of certain number of steps is saved depending on the saving rate value, which should be higher than the number of parameters.

As it has already been mentioned, the way the parameter space is explored is similar to Gibbs sampling, widely used to find the possible molecular configurations of a determined system at a given temperature using the classical Monte Carlo method. In that case, the values of physical constants such as the potential energy will in fact be a PDF related to all the configurations explored by the Monte Carlo method. In the case that concerns us, this technique provides certain advantages, both for the fitting and the posterior analysis

In the fitting process, the Bayesian method is able to accept a new set of parameters that increase  $\chi^2$  if this change is compatible with the experimental error, and therefore does not get stuck in local minima as the frequentist algorithms. In other words, the presented method is able to go *uphill* in the  $\chi^2\{P_i\}$  hypersurface.

In the second part, the exploration of the whole parameter space compatible with data using the MCMC method allows to find directly the probability density function associated with the likelihood for both the figure of merit  $\chi^2$  and the parameters, taking into account possible correlations between them, or minima not describable by a quadratic approximation. Furthermore, it is possible to obtain an explicit representation of the correlation between two parameters just by plotting their chains, one depending on the other.

## 2.4 Model selection

Experimental data can usually be described by more than one hypothesis, each implying a different physical mechanism to explain experimental results. For a successful analysis of data there is an obvious question that must be answered before going ahead, which of these possible models is better for explaining the obtained results? Model selection refers to decide which mathematical model is most suitable to fit the experimental data when there is uncertainty within a set of alternative models. Of course, we would have to choose a functional form based on the relevant background information available. This could include theoretical considerations, the results of calibration measurements or merely an approximation to simplify the algebra.

Commonly, the model selection criteria used is that a given model is better than others because it provides a “better fit” to the available data, understanding as a “better fit” that one which carries to a lower cost function value. However, this criteria is only true when the number of parameters across models is the same and all parameters remain uncorrelated. A model with more parameters usually gives a better fit to the data, and, thus, we must be careful to assess whether the data and their associated

errors support the new model.

Usually, frequentist methods use the figure of merit  $\chi_{red}^2$ , already introduced in section 2.1, for performing model selection and taking into account the number of parameters. Therefore, if two models fit the data equally successful (the same  $\chi^2$ ), the model with less parameters (with the smallest  $\chi_{red}^2$ ) will be favored. This is a way of quantifying the Ockham's razor principle: it is necessary to shave away unnecessary assumptions (parameters in our case). However, there is a better way to perform a model selection based on the cost function  $\chi^2$  probability density function, which also considers the number of degrees of freedom.

Model selection performed by using  $\chi_{red}^2$  makes the main assumptions involving frequentist approach, which have been commented in chapter 1: we suppose that there is a single minimum in  $\chi^2$ , that this minimum has parabolic dependence on all parameters and that there are no correlations between parameters. In fact, if these three assumptions are accomplished, the probability density function of  $\chi^2$  is given by the following expression [9]:

$$P(\chi^2) \propto (\chi^2)^{\frac{N}{2}-1} \cdot e^{-\frac{\chi^2}{2}} \quad (2.11)$$

where N is simply the number of parameters of the mathematical model. Fig. 2.2 shows the  $\chi^2$  PDF for increasing degrees of freedom (number of model parameters), defined by the previous analytical expression. Eq. 2.11 has a term independent from the number of parameters,  $e^{-\chi^2/2}$ , that decreases together with the quality of the fitting or when the error associated with the experimental data,  $\sigma_k$ , increases. The term  $(\chi^2)^{\frac{N}{2}-1}$  increases exponentially with the number of parameters, displacing the maximum of the distribution to higher values of  $\chi^2$ . These terms are shown separately in the inset of the figure.

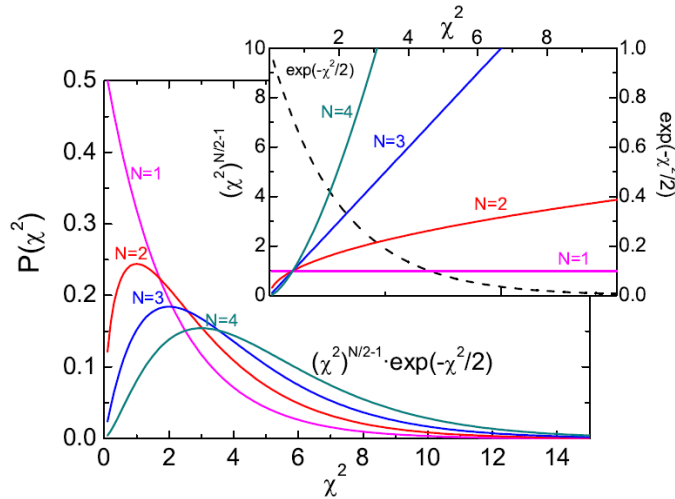


FIGURE 2.2:  $\chi^2$  distribution (eq. 2.11) for an increasing number of fitting parameters N. The inset shows the terms associated to the quality of the fit (dashed line) together with the one depending on the number of parameters (colored lines)

As it has already been commented, there is a criteria for performing model selection based on the  $\chi^2$  PDF, and it consists in looking for the model with the  $\chi^2$  PDF maximum at a lowest value. This way, the aforementioned preference for the model with the minimum number of parameter when alternatives lead to the same value of  $\chi^2$  is now approach based on probability theory, instead on the figure of merit  $\chi_{red}^2$ .

Meanwhile expression 2.11 is obtained under frequentist assumptions, Bayesian algorithms such as FABADA finds  $\chi^2$  PDF in a natural way by directly exploring the parameter space without any supposition and having into account parameter correlations. Certainly, the obtained PDF will in general not exactly follow the distribution described by eq. 2.11, despite being quite similar.

Therefore, using the probability density function criteria through the graphs obtained by FABADA algorithm allows to get conclusions about model selection without the drawback of assuming any frequentist supposition.



## Chapter 3

# Mantid Implementation

The Mantid project provides a framework that supports high-performance computing and visualization of scientific data. The aim of the Mantid framework is to provide a single platform for data reduction and analysis of neutron and muon scattering data across instruments and facilities across the world. Currently it has three main partners, ISIS, SNS and HFIR, but more partners, such as ILL, PSI and MacStas have joined recently. Mantid is an open source software supported by multiple target platforms, as Windows, Linux and Mac [12]. Despite being created to manipulate and analyse Neutron and Muon scattering data, it could be applied to many other techniques.

Mantid Project started in 2007 and, even though it is currently used in all the ISIS instruments, it is in a continuous development and it is being improved across versions. In fact, apart from data reduction and typical analysis, it is being extended with more and more interfaces and algorithms for data interpretations and visualizations.

Under the idea of extending the features of Mantid application software, this works implements into Mantid the algorithm for Bayesian analysis FABADA. The aim is it to become a powerful tool taking advantage of Mantid interfaces, manipulation of data files and results visualization. The algorithm basics explained in chapter 2 must be coded as part of the Mantid framework and adapting each part to the way that Mantid internal performance works (reading data, evaluating functions, interacting with interfaces, saving and visualizing results, etc.).

In the following section, we are going to show briefly how it is the FABADA interface and how to manage it to perform a fitting, as well as which results are obtained. Throughout it, there will be several images in order to illustrate everything that is being explained. In fact, it will be analysed experimental data corresponding to the Cl-Adamantane QENS experiment<sup>1</sup> corresponding to chapter 6.

We are not going into any detail about the code underling the software development, nevertheless as it is free software you can find the complete framework code in the Mantid Project GitHub main repository (<https://github.com/mantidproject/mantid>). Moreover, Mantid Project also has a Doxygen code documentation page (<http://doxygen.mantidproject.org/nightly>) where, beyond all the code files involved with FABADA, there is also a deep documentation about them. Otherwise, as mentioned, the following is just a brief summarize, for more information about how to use FABADA in Mantid consult its manual.

---

<sup>1</sup> In particular, it is going to be analysed the spectrum  $S(\mathbf{Q}, w)$  corresponding to  $\mathbf{Q} = 0.75 \text{ \AA}^{-1}$  of the measurement at 300 K

### 3.1 Using FABADA within Mantid

Previous versions of Mantid already had implemented fitting algorithms such Levenberg-Marquardt or BFGS. These algorithms received the name of minimizers and could be found in the Mantid's *Fit Function* menu. Therefore, in order to make the things easier for the user, the option to use FABADA is allocated in the same place.

#### 3.1.1 The visual interfaces

Fig 3.1 shows the Mantid's main window, where there are two menus that are which really matter to us, *Workspaces* and *Fit Function*.

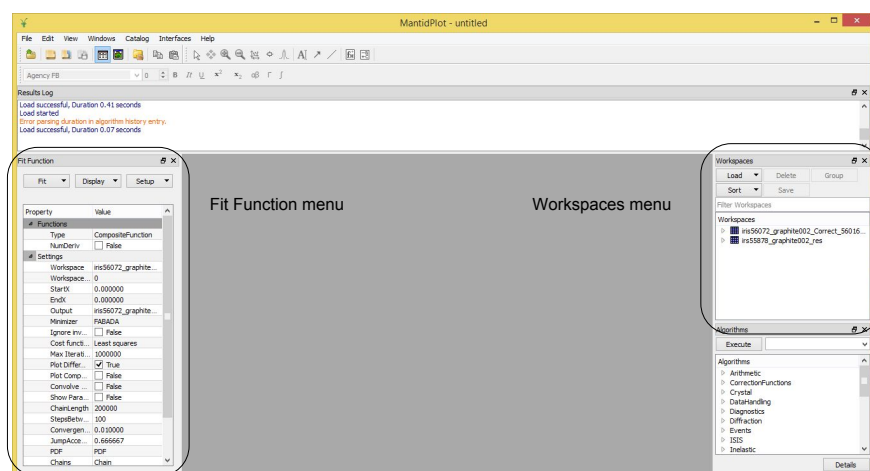


FIGURE 3.1: Mantid's main window where *Fit Function* and *Workspaces* menus have been highlighted.

The first step is to load the data file with the experimental results, and the way to do that is through the *Workspaces* menu. Once the file is loaded, it is possible to open the workspace and plot the data we are going to work with.

The next step is to set the fitting function, which corresponds to the mathematical model we want to use for the fitting. In the *Fit Function* menu, there is the option *Add Function* which allows the user to choose from a huge variety of functions (most of them related with neutron and muon scattering analysis, but also some quite more general). This browser also allows to create a composite function from more than one function and to convolve a resolution file of data with the fitting function. There is also the option of writing directly the function to use, if you have not enough with the default defined ones. Fig. 3.2 shows how the Fit Function menu looks like once a quite complex function has been added.

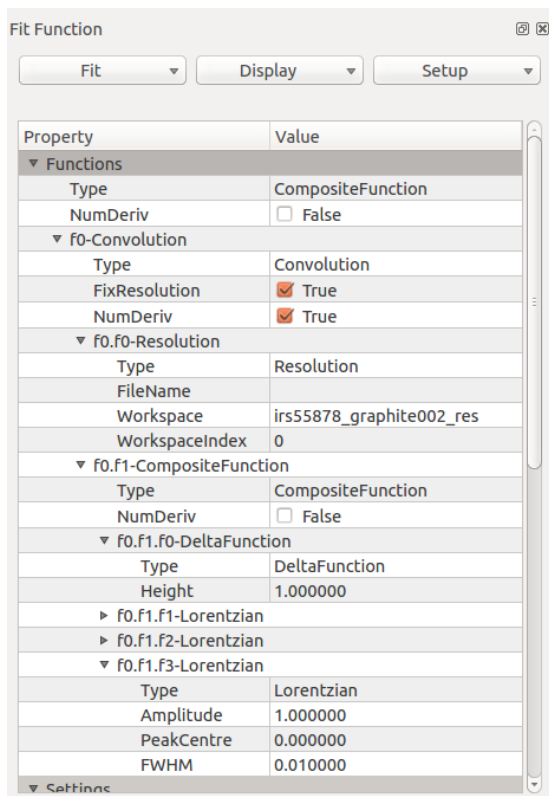


FIGURE 3.2: Fit Function menu with the function  $Res \otimes (\delta + L_1 + L_2 + L_3)$  added. Where  $Res$  is a data file acting as Resolution,  $\delta$  is a Dirac's delta function and  $L_n$  are Lorentzian functions.

In the same *Fit Function* menu must be indicated which workspace we want to analyze and which minimizer to use. Once FABADA is chosen, there appear some new setting options (see fig. 3.3). These specific options are parameters related with the algorithm performance explained in 2.2, and the user is who manage them:

- **Chain Length:** number of total steps (eq. 2.7) done by the algorithm once all the fitting function parameters have converged.
- **Saving Rate:** the algorithm saves one value each certain number of steps in order to create a shorter chain (with uncorrelated sets of parameters) which will be the chain to analyze and obtain results. *Saving Rate* parameter is this certain number of steps.
- **Convergence Criteria:** the maximum relative variation of the cost function, due to the variation of one parameter, that will be considered as the corresponding parameter has converged (eq. 2.10). Default value of 0,1
- **Jump Acceptance Rate:** desired percentage of acceptance for new parameters ( $R_{desired}$  in eq. 2.9). Default value of 0,666.

Moreover, the user has one more option in the *Fit Function* menu, the possibility of naming (see fig. 3.3) the different workspaces created by FABADA with the resulting information. In the following section we will take a look to what these workspaces are, which information they contain and how they look like.

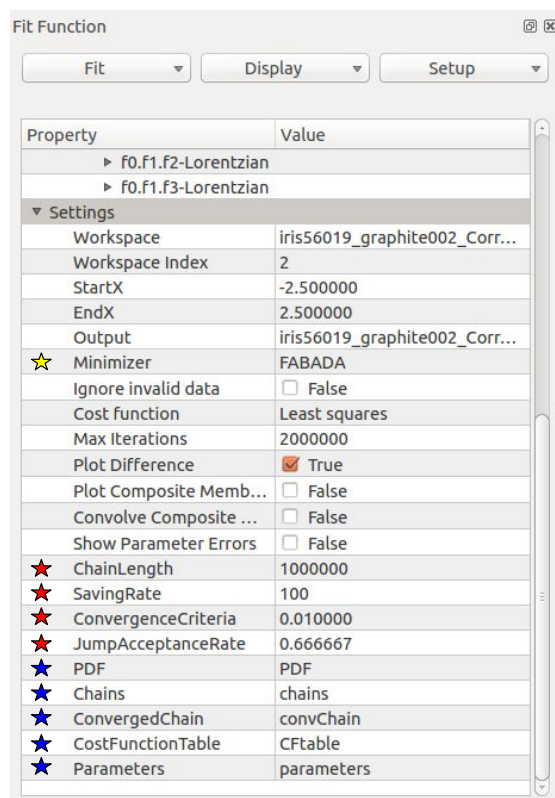


FIGURE 3.3: Fitting settings in the *Fit Function* menu. *Yellow star*: minimizer's choice. *Red stars*: parameters related with FABADA algorithm performance. *Blue stars*: naming the resulting workspaces.

Therefore, once the function and the fittings settings are properly set up, we can carry out the fitting. In the *Results Log* window on the top (see fig. 3.1) will appear any comment regarding the fitting, warning and fitting duration.

### 3.1.2 A look to the results

As commented at the beginning of the chapter, for illustrating the explanation it is going to be used a real example corresponding to the CI-Adamantane experiment (chapter 6). At this point, it is relevant to mention that for that fitting has been used a *Chain Length* value of 200000 and a *Saving Rate* value of 100.

In the same way that when using the other minimizers, it is created a workspace with the resulting fitting function evaluated in the same range as the experimental data. Plotting this workspace we can visually evaluate the quality of the fit (fig. 3.4).

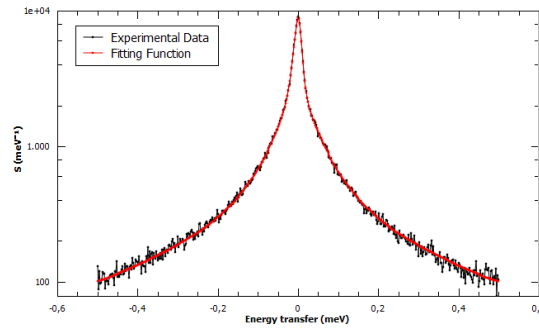


FIGURE 3.4: Fit to the experimental data (black line) of the fitting function (red line) defined in 3.2

Furthermore, when performing a fitting with FABADA, different specific workspaces are generated with all the information about the results, but also about the process. These workspaces are the followings:

- **Chains:** it contains the value of each parameter and of the cost function for each step of the algorithm. These chains show the fitting process from the parameters (and cost function) initial value until the convergence, as well as the MCMC chain generation.

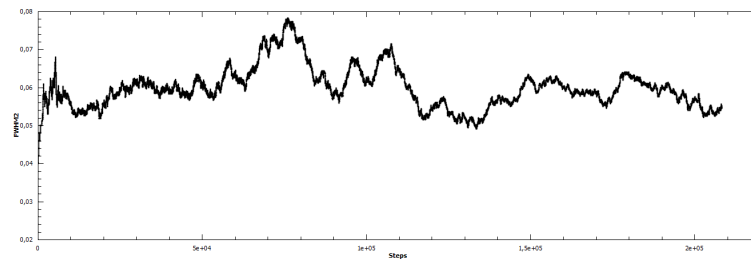


FIGURE 3.5: Chains workspace plot for parameter FWHM2. As it contains both the fitting part and the MCMC generation, the total number of steps is bigger than 200000.

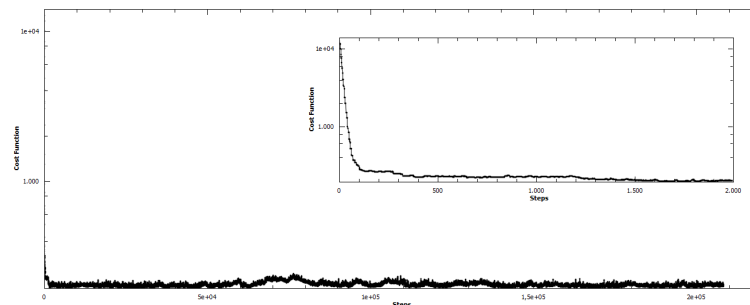


FIGURE 3.6: Chains workspace plot for the  $\chi^2$  cost function with logarithmic Y axis. The inset shows only the first 2000 steps in order to better appreciate the convergence of the  $\chi^2$  value.

- **Converged Chains:** it only contains the converged part of the total chain and one value for each certain number of steps (depending on the *Saving Rate* parameter). The length of these chains is the value of the parameter *Chain Length* divided by the *Saving Rate* value. These are the chains that actually FABADA uses to obtain other results as the PDFs.

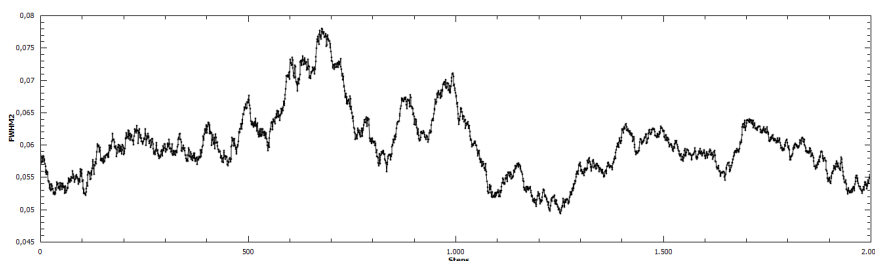


FIGURE 3.7: Converged Chains workspace plot for parameter FWHM2. As *Chain Length* is 200000 and a *Saving Rate* is 100, the length of this workspace equals to 2000.

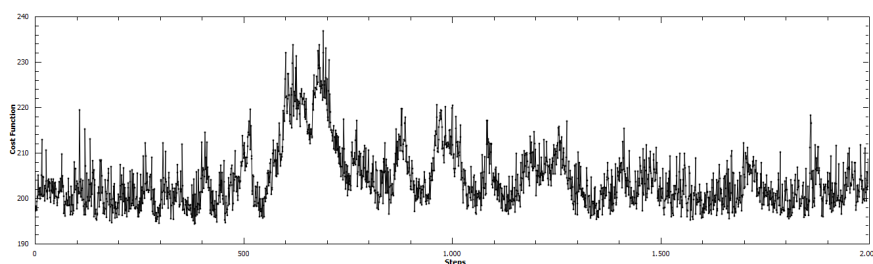


FIGURE 3.8: Converged Chains workspace plot for the  $\chi^2$  cost function. It is possible to appreciate how between steps 600<sup>th</sup> and 700<sup>th</sup>, the MCMC generation has fallen in a relative minimum.

- **PDF:** it contains the Probability Density Function for each function parameter and for the cost function.

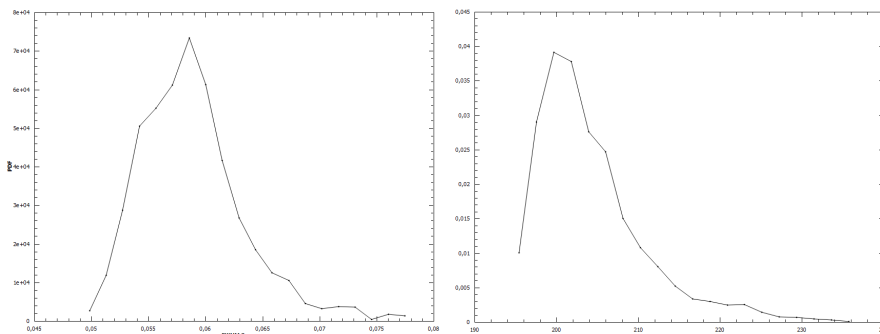
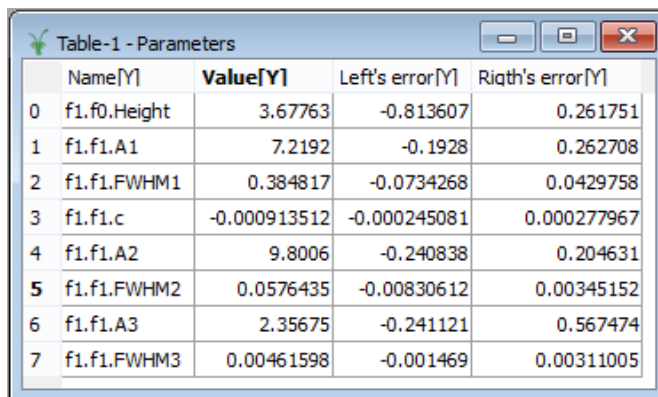


FIGURE 3.9: PDF plot for the FWHM2 parameter (left) and for the  $\chi^2$  cost function (right).

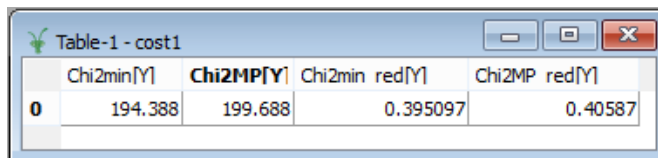
- **Parameter Errors:** a table which contains the best value and the errors for each function. As commented in section , the errors can be no symmetric.



	Name[Y]	Value[Y]	Left's error[Y]	Riqth's error[Y]
0	f1.f0.Height	3.67763	-0.813607	0.261751
1	f1.f1.A1	7.2192	-0.1928	0.262708
2	f1.f1.FWHM1	0.384817	-0.0734268	0.0429758
3	f1.f1.c	-0.000913512	-0.000245081	0.000277967
4	f1.f1.A2	9.8006	-0.240838	0.204631
5	f1.f1.FWHM2	0.0576435	-0.00830612	0.00345152
6	f1.f1.A3	2.35675	-0.241121	0.567474
7	f1.f1.FWHM3	0.00461598	-0.001469	0.00311005

FIGURE 3.10: Parameters Errors workspace with all the resulting values for the example being exposed throughout this chapter.

- **Cost Function:** a table with the cost function minimum and most probable values. The reduced values, as defined in eq. 2.2, are also given.



	Chi2min[Y]	Chi2MP[Y]	Chi2min red[Y]	Chi2MP red[Y]
0	194.388	199.688	0.395097	0.40587

FIGURE 3.11: Cost Function workspace, corresponding to the  $\chi^2$  PDF shown in 3.9

### 3.1.3 Writing a Python script

Using FABADA through Mantid interfaces and menus is not the user's only option. It is also implemented the possibility of calling the algorithm internally by executing a Python script from the *Mantid's Script Window*. This practice implies certain advantages, for example it is possible to write a script to perform different fittings consecutively without being changing every time the elements from the browsers. It is also a way to keep saved what fittings have been performed in order to, maybe, carry out them for different experimental data or adding little changes in a future.

The main steps to write a Python script for calling FABADA are the same as the ones followed in section 3.1.1 with the Mantid interfaces. Following, there is an example for fitting the same Cl-Adamantane data which results are shown in the previous section 3.1.2:

- Loading the experimental and resolution data:

```
data_path = 'C:\Users\Diego\Documents\ISIS\ClAda'

ws_data = Load(Filename=data_path+'\iris56072_graphite002_Correct_56016_red.nxs')
ws_res = Load(Filename=data_path+'\irs55878_graphite002_res.nxs')
```

- Defining the fitting function, three Lorentzians convolved with the resolution data in this case:

```
function_str="(composite=Convolution,FixResolution=true,NumDeriv=true;name=Reso
lution,Workspace=ws_res,WorkspaceIndex=0;(name=DeltaFunction,Height=1;name=Lore
ntzian,Amplitude=1,PeakCentre=0,FWHM=0.5;name=Lorentzian,Amplitude=1,PeakCentre
=0,FWHM=0.05;name=Lorentzian,Amplitude=1,PeakCentre=0,FWHM=0.005))"
```

- Setting FABADA minimizer and its parameters:

```
minimizer_str="FABADA,ChainLength=1000000,StepsBetweenValues=100,ConvergenceCri
teria=0.001,JumpAcceptanceRate=0.66666,PDF=PDF_L3,Chains=Chains_L3,ConvergedCha
in=Converged_L3,CostFunctionTable=CFTable_L3,Parameters=Parameters_L3"
```

- Calling the function *Fit()* in order to start the fitting:

```
Fit(Function=function_str,InputWorkspace=ws_data,WorkspaceIndex=3,StartX=-0.54,
EndX=0.54,CreateOutput=True,Output='L3',OutputCompositeMembers=True,MaxIteratio
ns=1500000,Minimizer=minimizer_str)
```

## 3.2 Conclusions and prospects

The work presented in this chapter is the fulfillment of the adaptive Markov chain Monte Carlo introduced in chapter 2 into a usable software tool. The Bayesian algorithm implemented allows control over certain fitting settings, in fact, it is possible to control the chain length that will be created, the saving rate for avoiding correlation between the parameter sets of that chain, the thoroughness of the convergence criteria and even the desired acceptance for the parameter jump, which directly affects the jump tuning.

One of the main benefits of the implementation of the algorithm in a platform such as Mantid is the possibility of using it with whatever experimental data file, due to the huge variety that Mantid is able to interpret. Moreover, Mantid also provides with the possibility of using whatever fitting function, even to use a model that needs to convolve a mathematical function with a resolution file of data. These features makes the implemented algorithm able for whatever purpose the user could have. Furthermore, the user-friendly interface that Mantid provides for using FABADA makes it even more attractive.

The way that the results are saved through workspaces provides a useful way to manage them, as they can be directly plotted with Mantid or saved into an ASCII file with any extension, in order to manage and plot them with other software. In fact, something that can, and should, be improved in the FABADA implementation is the graphical representation of the Probability Density Functions. As it has been explained in section 2.4, PDFs are crucial for performing model selection, however, as it can be observed in fig. 3.9, the binning for the PDF plots is not optimized and that leads to sharpened and ugly plots. It is possible to obtain much better plots for the PDFs from the data contained in the *Converged Chain* workspace and, in fact, the PDFs that will appear in chapters 4 and 6 have been gotten plotting the results with a specific program for doing that.

Finally, once that FABADA is implemented into Mantid, it is possible to think in possible improvements than can be made for taking the most from Bayesian analysis. One possibility is to add the option of performing what is called a simulated annealing. It consists in redefining the cost function  $\chi^2$  in order the algorithm to be able to avoid getting stuck even in the case when the barriers in the  $\chi^2\{P_i\}$  hypersurface are greater than those associated to experimental error. For that, it is necessary to go back to the comparison of the Gibbs sampling technique for finding molecular configurations we did in section 2.3. It is possible to relate energy to  $\sum_{k=1}^n (H_k - D_k)^2$ , which is the magnitude giving information about the fit quality, and temperature to the data associated error ( $T \approx \sigma^2$ ). Then, it is used a fictitious cost function  $\chi^2 = \sum_{k=1}^n \frac{(H_k - D_k)^2}{T\sigma^2}$  where  $T$  is a constant defined to artificially increase the experimental error, which is named as *temperature* by similitude with classical Montecarlo simulations. Fittings are then started at high temperature, and the system is relaxed by lowering the temperature up to  $T = 1$ .



## Chapter 4

# How many lines are there?

Once the Bayesian algorithm FABADA is fully implemented in Mantid software, we are going to illustrate its potential. In order to do that, in this chapter we are going to deal with an issue that occurs frequently in spectroscopy, crystallography and many other areas of science. The case is to assess how many signal peaks describes a pertinent set of data. This is an old question posed by D. S. Sivia and C. J. Carlile in their seminal study *Molecular spectroscopy and Bayesian spectral analysis - How Many Lines are there?* [13].

Quasielastic Neutron Scattering (QENS) is often complicated by the fact that a number of dynamical processes are all centered on the elastic response of the material, and the number of these processes is usually unknown. When the timescales associated with these processes are quite different, it is possible to get an approximate idea through visual inspection. However, when spectral widths become comparable between them, the situation becomes confuse. To address this question in a systematic manner, synthetic QENS data is going to be generated with a certain number of peaks, and then, the Bayesian algorithm implemented into Mantid will be used to fit this data considering different number of components. A model selection will be performed with the resulting  $\chi^2$  probability density functions in order to ascertain if the results agree with the information we already knew.

The study presented below have been published in the *Journal of Physics: Conference Series* with the title: *FABADA goes MANTID to an Answer an Old Question: How Many Lines Are There?* [5].

### 4.1 Data generation

In QENS analysis, each quasielastic component related with a dynamic process is approached by a Lorentzian function. Therefore, in our study, each peak has been considered as a Lorentzian ( $L$ ) function, defined by the following expression:

$$L = \frac{A}{\pi} \left( \frac{\frac{FWHM}{2}}{(x - x_0)^2 + \left(\frac{FWHM}{2}\right)^2} \right) \quad (4.1)$$

where FWHM refers to parameter Full-Width-Half-Maximum,  $A$  to the amplitude and  $x_0$  to the peak center.

Synthetic QENS data has been generated as the linear addition of three equally weighted Lorentzian modes convolved with a Resolution function:

$$R \otimes (L_1 + L_2 + L_3) \quad (4.2)$$

where resolution  $R$  has been simulated by a Gaussian peak with a FWHM of 0.01 meV, since Gaussian peak is which best describes resolution for instruments used in QENS measurements. The mathematical expression for a Gaussian peak is given by:

$$G = H \cdot e^{\left(-\frac{(x-x_0)^2}{2\sigma^2}\right)} \quad (4.3)$$

It can be easily demonstrated that the Full-Width-Half-Maximum for a gaussian peak follows the expression  $FWHM = 2\sqrt{2\ln(2)} \cdot \sigma$ . Therefore, the resolution used in eq. 4.2 is:

$$R = e^{\left(-\frac{4\ln(2) \cdot x^2}{0.01^2}\right)} \quad (4.4)$$

where parameter height  $H$  has been set to one and, as a proper resolution expression, the peak is centered, so  $x_0$  equals zero. Parameters values for the different Lorentzian modes of eq. 4.2 are tabulated below

Peak	A	FWHM	$x_0$
$L_1$	1	0.04	0
$L_2$	1	0.4	0
$L_3$	1	2	0

TABLE 4.1: Parameters values for Lorentzian peaks in eq. 4.2

The same value for all amplitudes corresponds to the previously introduced concept that all three peaks are equally weighted. It also can be deduced from table 4.1 that all three Lorentzian peaks are centered, as corresponding to QENS spectra.

In order to emulate realistic experimental conditions, a Gaussian-distributed relative error of 6% has been added to the generated spectrum after convolution. The final resulting synthetic data is shown in fig. 4.1.

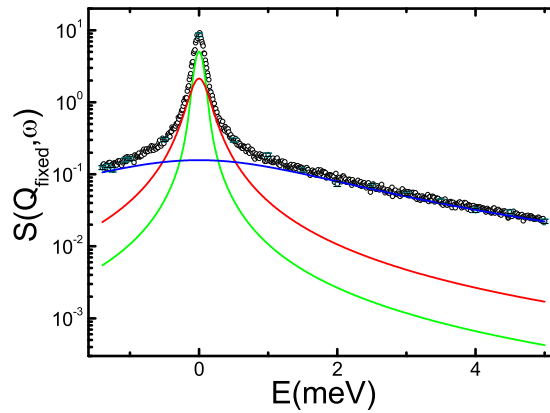


FIGURE 4.1: Synthetic QENS spectrum generated (circles). Green, red and blue lines corresponds to  $L_1$ ,  $L_2$  and  $L_3$  from eq. respectively

## 4.2 Model selection

Synthetic data is going to be analyzed considering 5 different models, each one described by an increasing number of Lorentzian modes, from 1 up to 5, hereafter denoted as  $L_n$  where  $n$  is the number of  $L$  peaks (do not confuse with the notation of eq. 4.2, where  $L_1$ ,  $L_2$  and  $L_3$  meant three different peaks). Once the five fittings are performed with FABADA, it is possible to use the criteria explained in section 2.4 for determining which model is the most appropriate. All the fittings will be carried out under the same conditions, standing out a *Chain Length* of 1 000 000 points with a *Saving Rate* of 100. Thereby we obtain a high enough amount of values for obtaining a smooth PDF shape for each fitting.

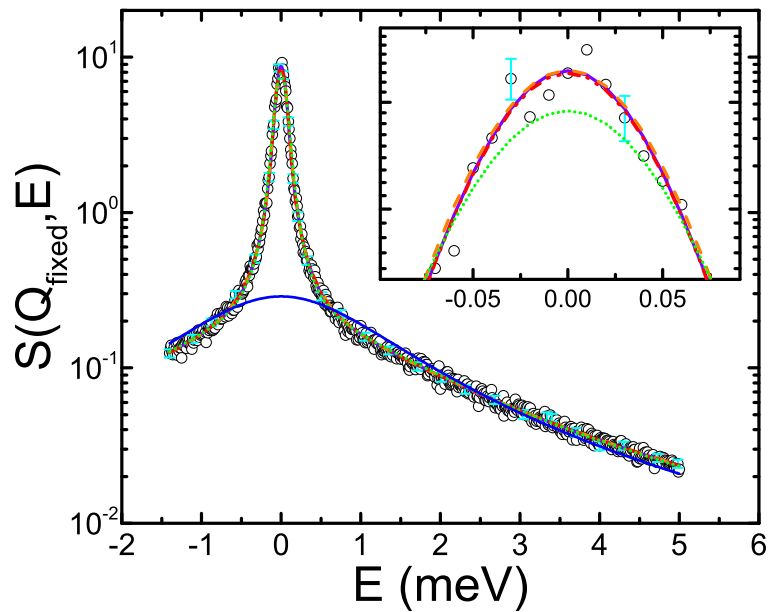


FIGURE 4.2: Fits to the synthetic QENS data (black circles) using an increasing number of  $L$  modes:  $L_1$  (solid blue line),  $L_2$  (dotted green),  $L_3$  (dashed-dot red),  $L_4$  (dashed orange), and  $L_5$  (solid purple). Note the logarithmic (linear) scales on the main figure (inset).

Visual inspection of fig. 4.2 makes it clear that it is not possible to describe the data with a model which only considers one Lorentzian peak. Beyond this case, a cursory visual analysis of these results does not provide any other conclusion. A much closer look at specific regions of the graph might still allow us to discover that  $L_2$  is slightly not as suitable model as the followings (see inset). However, for  $L_3$ ,  $L_4$  and  $L_5$  the quality of the fits remains virtually unchanged. At this point, it is when it is needed to look to the  $\chi^2$  Probability Density Functions:

Fig. 4.3 supports the discussion above about discarding model  $L_1$ , since the most probable value for its  $\chi^2$  PDF is at  $\chi^2 \approx 14305$ , more than one order of magnitude above the other models.  $L_2$  must also be discarded due to its  $\chi^2$  most probable value is yet clearly higher than the other models.

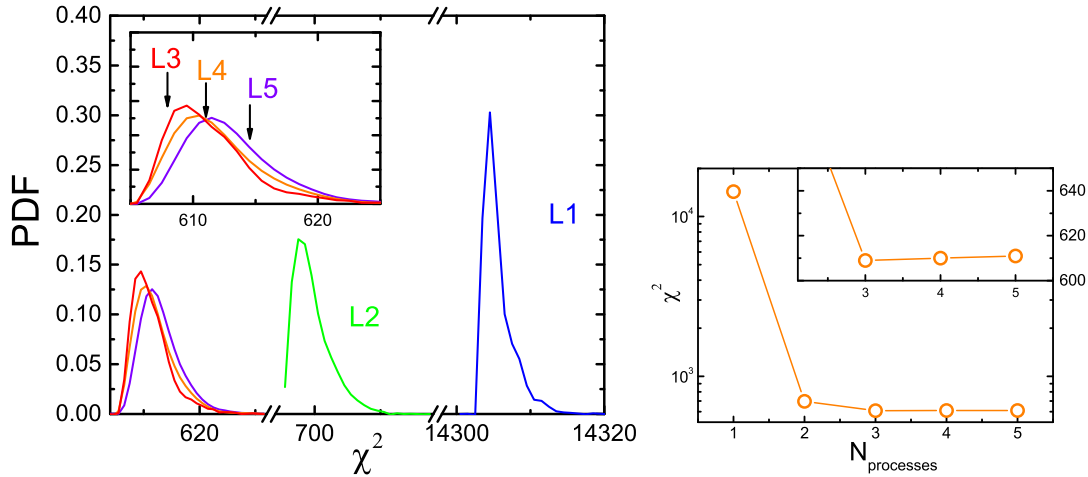


FIGURE 4.3: *Left*)  $\chi^2$  PDFs for models  $L_1$ - $L_5$ , the inset shows an enlargement around  $L_3$ - $L_5$ . This figure uses the same color coding as in fig. 4.2. *Right*) Most probable values of the  $\chi^2$  PDFs. Note the logarithmic (linear) scale in the main panel (inset).

For  $L_3$ ,  $L_4$ , and  $L_5$ , we see that the three PDFs share the same onset corresponding to the lowest  $\chi^2$  (best fit), as expected from the results shown in Fig. 4.2. However, the maximum of the PDF shifts to higher  $\chi^2$  values in going from  $L_3$  to  $L_5$ . This trend is a consequence of an increase in the number of parameters, leading to an overall broadening and therefore an upward shift of the corresponding  $\chi^2$  PDF. Thus, the addition of more parameters beyond  $L_3$  is clearly not justified by the experimental data. Model  $L_3$  has been quantitatively chosen as the best for describing the data.

From a physical viewpoint, it is interesting to pay attention to the situation related to the differences between  $L_2$  and  $L_3$ . As shown in fig. 4.3, the  $L_2$  PDF does not overlap with the corresponding one for  $L_3$ . In probabilistic terms, the immediate consequence of this result is that no combination of  $L_2$  parameters can provide a better fit than  $L_3$ . Therefore,  $L_3$  is favored over  $L_2$ , a result that we have established in a robust and quantitative manner.

### 4.3 Conclusions

The presented study shows how the Bayesian fitting algorithm FABADA enables robust data fitting and model selection well beyond more popular and widespread data-analysis methodologies. To illustrate it, we have revisited an old (yet still topical) question relating to the number of spectral modes present in QENS data, and the results have been completely satisfactory.

The criteria used has conclude that the addition of more components beyond  $L_3$  is clearly not justified by the analysed data, despite other models are able to get fits as good as with  $L_3$  model ( $L_3$  and  $L_3$  led to the same  $\chi^2$  minimum value). We would like to emphasize the fact that the method followed for obtaining the  $\chi^2$  probability density functions of fig. 4.3 does not rely on any assumptions relating to the shape of the underlying  $\chi^2$  landscape or possible correlations between parameters.

## Chapter 5

# Neutron scattering overview

There exist different experimental techniques based on the physical process of neutron scattering, the scattering of free neutrons by matter. These techniques are widely used in fields such as crystallography, physical chemistry, biophysics and, of course, materials research. Neutron scattering is the technique of choice for condensed matter investigations because it is a non-invasive probe, they do not change the investigated sample since they do not deposit energy into it. Moreover, one of the main advantages is that neutrons interact through nuclear interactions, therefore they have high penetration for most elements, not as X-rays which interacts with the electron cloud of atoms. Essentially we can differentiate between two main types, elastic neutron scattering (also referenced as neutron diffraction) and inelastic neutron scattering (also called neutron spectroscopy).

On the one hand, neutron diffraction allows to determine the atomic and/or magnetic structure of a material, either crystalline solids, liquids, gasses or amorphous materials. The sample to be examined is hit by a beam of thermal or cold neutrons, the neutrons exiting the experiment maintain more or less the same energy as the incident neutrons. Taking advantage of neutron's wave properties, structure information is deduced from the intensity pattern around the sample. The technique is similar to X-ray diffraction but due to their different type of radiation, they provide complementary information.

On the other hand, inelastic neutron scattering measures the change in the neutron energy that occurs in the collision with the sample. A wide variety of physical phenomena such as diffusional or hopping motions of atoms, rotational modes of molecules, molecular vibrations, recoil in quantum fields or magnetic and quantum excitations can be probed using this technique. There are different ways to perform this kind of experiments, in section 5.3.1 we will go deeper in the time of flight technique. Anyway, the resulting information is generally communicated through the dynamic structure factor (also called inelastic scattering law)  $S(\mathbf{Q}, w)$ , which will be introduced in the following section. When energy transfers are close to zero the technique receives the name of quasielastic neutron scattering (QENS).

### 5.1 Coherent and incoherent scattering

Assuming a current of  $I_0$  neutrons per second and per surface incident on the sample, and  $N_S$  the total number of neutrons scattered per second<sup>1</sup>, it is possible to define the

---

<sup>1</sup>Neutrons that are not scattered are absorbed by the sample leading to compound nucleus in an excited state. When the nucleus decay to their ground state again, it could occur the emission of  $\gamma$  radiation or charged particles such as  $\alpha$  particles or tritons.

scattering cross-section  $\sigma_s$  through the relation

$$N_S = I_0 \cdot \sigma_s \quad (5.1)$$

where  $\sigma_s$  has the dimension of a surface.  $\sigma_s$  can be understood as the probability that a neutron is scattered (and not absorbed) when hitting that particular sample.

Moreover, we can define the double-differential cross section as:

$$\frac{\partial^2 \sigma}{\partial \Omega \partial E} = \frac{1}{\hbar} \frac{\partial^2 \sigma}{\partial \Omega \partial w} \quad (5.2)$$

which gives the probability that a neutron, with incident energy  $E_0$  (monochromatic beam), leaves the sample in the solid angle element  $d\Omega$  about the direction  $\Omega$  and with a final energy between  $E$  and  $E + dE$ . This cross-section is the quantity actually measured in an inelastic scattering experiment.

Following the notation and development pursued by M. Bée in his masterpiece *Quasielastic Neutron Scattering* [14], the double-differential cross section can be expressed as:

$$\frac{\partial^2 \sigma}{\partial \Omega \partial w} = \frac{k}{k_0} \frac{1}{2\pi N} \sum_i \sum_j \int_{-\infty}^{\infty} \langle b_i e^{i\mathbf{Q} \cdot \mathbf{R}_i(t)}, b_j e^{-i\mathbf{Q} \cdot \mathbf{R}_j(0)} \rangle e^{-iwt} dt \quad (5.3)$$

where  $k_0$  is the wavevector of the impinging monochromatic neutron beam of energy  $E_0$ ,  $k$  is the final wavevector and  $\mathbf{Q}$  is defined as  $\mathbf{k} - \mathbf{k}_0$  (neutron-wavevector transfer). Vector  $\mathbf{R}_i(t)$  is simply the position of the nucleus  $i$  of the sample at time  $t$  and  $N$  is the total number of nuclei. Scattering length  $b$  is a parameter which varies from one nucleus to another owing to nuclear spin and the presence of isotopes. For the following discussion is enough to assume there is no correlation between the  $b$  values of different nuclei, therefore we can obtain that  $\overline{b_i b_j} = (\bar{b})^2$  for  $i \neq j$  and  $\overline{b_i b_j} = \overline{b^2}$  for  $i = j$

The sum over all  $i, j$  suggests that we are overlaying two different measurements. The information about a single particle movement when  $i = j$  and the information about different particles when  $i \neq j$ . With the proper mathematical development expression 5.3 can be expressed as the sum of two different terms:

$$\frac{\partial^2 \sigma}{\partial \Omega \partial w} = \left( \frac{\partial^2 \sigma}{\partial \Omega \partial w} \right)_{coh} + \left( \frac{\partial^2 \sigma}{\partial \Omega \partial w} \right)_{inc} \quad (5.4)$$

with:

$$\left( \frac{\partial^2 \sigma}{\partial \Omega \partial w} \right)_{coh} = \frac{\sigma_{coh}}{4\pi} \frac{k}{k_0} \frac{1}{2\pi N} \sum_i \sum_j \int_{-\infty}^{\infty} \langle e^{i\mathbf{Q} \cdot \mathbf{R}_i(t)}, e^{-i\mathbf{Q} \cdot \mathbf{R}_j(0)} \rangle e^{-iwt} dt \quad (5.5)$$

$$\left( \frac{\partial^2 \sigma}{\partial \Omega \partial w} \right)_{inc} = \frac{\sigma_{inc}}{4\pi} \frac{k}{k_0} \frac{1}{2\pi N} \sum_i \int_{-\infty}^{\infty} \langle e^{i\mathbf{Q} \cdot \mathbf{R}_i(t)}, e^{-i\mathbf{Q} \cdot \mathbf{R}_i(0)} \rangle e^{-iwt} dt \quad (5.6)$$

where  $\sigma_{coh} = 4\pi(\bar{b})^2$  and  $\sigma_{inc} = 4\pi(\overline{b^2} - (\bar{b})^2)$ . We see from the equations that the coherent scattering depends on the correlation between the positions of the same nucleus at different times, and on the correlation between the positions of different nuclei

at different times. It therefore gives interference effects. The incoherent scattering depends only on the correlation between the positions of the same nucleus at different times.

## 5.2 Correlation functions

In the following, we are going to relate the cross-sections for neutron scattering to thermal averages of operators belonging to the scattering system [15]. The thermal averages can be expressed in terms of what are known as *correlation functions*. The development refers to the case of a single component system.

Firstly, we define a function  $I(\mathbf{Q}, t)$ , known as the *intermediate function*, by

$$I(\mathbf{Q}, t) = \frac{1}{N} \sum_{i,j} \langle e^{i\mathbf{Q}\cdot\mathbf{R}_i(t)}, e^{-i\mathbf{Q}\cdot\mathbf{R}_j(0)} \rangle \quad (5.7)$$

and, from it, a function  $S(\mathbf{Q}, w)$  called *scattering function* or *scattering law* as

$$S(\mathbf{Q}, w) = \frac{1}{2\pi} \int_{-\infty}^{\infty} I(\mathbf{Q}, t) e^{-iwt} dt \quad (5.8)$$

It is quite interesting to mention that the function  $S(\mathbf{Q}, w)$  is related, by a inverse Space-time Fourier Transform, with the well-known *time-dependent pair-correlation function*

$$S(\mathbf{Q}, w) = \frac{1}{2\pi} \int G(\mathbf{r}, t) e^{i(\mathbf{Q}\cdot\mathbf{r}-wt)} d\mathbf{r} dt \quad (5.9)$$

which describes how, in a system of particles, density varies as a function of distance, and time, from a reference particle.

In a similar way as in expressions 5.7 and 5.8 we can define the *self-intermediate function*

$$I_{self}(\mathbf{Q}, t) = \frac{1}{N} \sum_i \langle e^{i\mathbf{Q}\cdot\mathbf{R}_i(t)}, e^{-i\mathbf{Q}\cdot\mathbf{R}_i(0)} \rangle \quad (5.10)$$

And the *incoherent scattering function*

$$S_{inc}(\mathbf{Q}, w) = \frac{1}{2\pi} \int_{-\infty}^{\infty} I_{self}(\mathbf{Q}, t) e^{-iwt} dt \quad (5.11)$$

The objective of these definitions is to rewrite the expressions for the double-differential cross sections 5.5 and 5.6 in order to depend on the scattering law

$$\left( \frac{\partial^2 \sigma}{\partial \Omega \partial w} \right)_{coh} = \frac{\sigma_{inc}}{4\pi} \frac{k}{k_0} \cdot S(\mathbf{Q}, w) \quad (5.12)$$

$$\left( \frac{\partial^2 \sigma}{\partial \Omega \partial w} \right)_{inc} = \frac{\sigma_{inc}}{4\pi} \frac{k}{k_0} \cdot S_{inc}(\mathbf{Q}, w) \quad (5.13)$$

All this theoretical development is because in chapter 6 we are going to analyze results from quasielastic neutron scattering experiments. The measurements collected corresponds to the scattering law  $S(\mathbf{Q}, w)$ , therefore it is important to know what it

means and whence it comes. It is also worth noticing that  $S_{inc}(\mathbf{Q}, w)$  is already contained in  $S(\mathbf{Q}, w)$ .

Basically,  $S(\mathbf{Q}, w)$  and  $S_{inc}(\mathbf{Q}, w)$  are quite different in nature. Indeed,  $S(\mathbf{Q}, w)$  involves a sum over the phase-shifts of different particles, and thus in interference effects. Meanwhile,  $S_{inc}(\mathbf{Q}, w)$  refers to the same particle position at different times 0 and t. The relative magnitude of  $S(\mathbf{Q}, w)$  and  $S_{inc}(\mathbf{Q}, w)$  mainly depends on the nature of the nuclei in the sample. If the system contains no hydrogen, then the spectra will be essentially coherent and will reflect collective atomic motions. Conversely, as soon as sample molecules contain hydrogen atoms, the scattering becomes incoherent. Hence, incoherent neutron scattering from organic hydrogenated molecules provides a powerful tool in the analysis of the motions of one individual proton and, consequently, of the dynamics of the molecules itself. In fact, the incoherent scattering function  $S_{inc}(\mathbf{Q}, w)$  in the elastic region is separable into a purely elastic component and a quasi-elastic component, which can be mathematically expressed by a Dirac's delta function for the elastic one and by a Lorentzian function for each dynamic process of the quasi-elastic component [16, 17].

$$S_{inc}(\mathbf{Q}, w) = A_0 \cdot \delta(w) + A_l \sum_{l=1}^n \frac{\Gamma_l}{w^2 + (\Gamma_l)^2} \quad (5.14)$$

### 5.3 IRIS instrument

IRIS is a high resolution quasielastic and inelastic neutron scattering spectrometer with long wavelength diffraction capabilities. In common with other instruments at a pulsed neutron source, IRIS uses the time-of-flight (TOF) technique for data analysis. It is an inverted or indirect geometry spectrometer such that neutrons scattered by the sample are energy analysed by means of Bragg scattering from one of two large single crystal arrays, pyrolytic graphite and muscovite mica. Each analyser is associated with its own bank of 51 ZnS scintillator detectors. The two analyser banks, which can operate simultaneously, afford high resolution over wide energy and momentum transfer ranges [19].

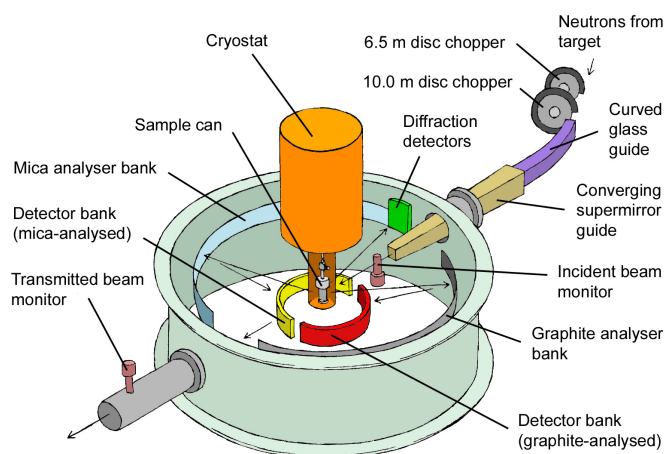


FIGURE 5.1: IRIS spectrometer schematic

Fig. 5.1 shows IRIS spectrometer, which consists of a 2 meters diameter vacuum vessel containing the two crystal analyser arrays and the two detectors banks, but also a diffraction detector bank at  $2\theta = 170^\circ$  containing ten Helium-3 gas tubes. Incident and transmitted beam monitors are located before and after the sample position respectively.

### 5.3.1 Principle of operation

During a quasielastic neutron scattering experiment, only those neutrons with the appropriate wavelength/energy to satisfy the Bragg condition are directed from the array of single crystals towards the detector bank (fig. 5.2). Then, energy gain or loss processes occurring within the sample may be investigated through the time-of-flight. TOF technique can be summarised mathematically as follows [18].

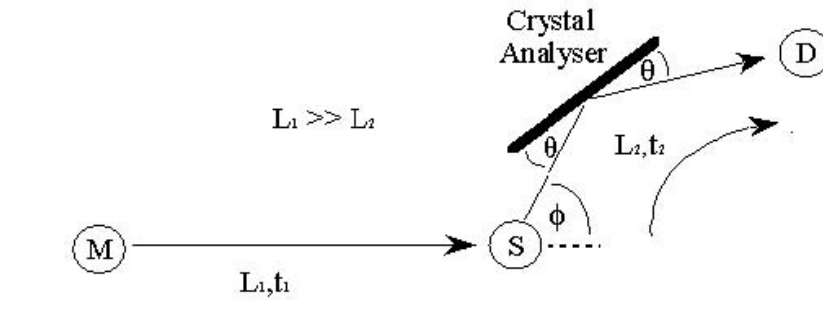


FIGURE 5.2: IRIS principle of operation schematic

The two disc choppers (see fig. 5.1), which are represented as a moderator M in the scheme 5.2, delimit the range of neutron energies incident upon the sample. Kinetic energy (classical mechanics) and momentum (de Broglie) are expressed like that:

$$E = \frac{1}{2}m_n v^2 \quad \text{and} \quad p = m_n v = \frac{h}{\lambda} \quad (5.15)$$

Consequently, the time of flight  $t_1$  of each neutron along the primary flight path  $L_1$ , from the moderator to the sample, is variable. However, since only those neutrons with a final energy,  $E_{final}$ , that satisfies the Bragg condition  $\lambda = 2d \sin \theta$  are scattered toward the detector bank, D, equations 5.15 can be reformulated to give:

$$E_{final} = \frac{1}{2}m_n \left(\frac{L_2}{t_2}\right)^2 = \frac{1}{2}m_n v^2 = \frac{p^2}{2m_n} = \frac{1}{2m_n} \left(\frac{h}{\lambda_a}\right)^2 = \frac{1}{2m_n} \left(\frac{h}{2d_a \sin \theta}\right)^2 \quad (5.16)$$

where  $d_a$  is the d-spacing of the analysing crystal. All instrument parameters are accurately known:  $d_a$ , angle  $\theta$  and distances  $L_1$  and  $L_2$  (fig. 5.2). Consequently, the time  $t_2$ , it takes for a detected neutron of energy  $E_2$  to travel the distance  $L_2$  from the sample position to the detector can be calculated using:

$$t_2 = \frac{2m_n L_2 d_a \sin \theta}{h} \quad (5.17)$$

Due to interaction of neutrons within the sample, they can gain or lose energy. By measuring the total time of flight  $t = t_1 + t_2$ , the energy exchange within the sample can be determined as:

$$\Delta E = E_{initial} - E_{final} = \frac{1}{2}m_n \left[ \left( \frac{L_1}{(t - t_2)} \right)^2 - \left( \frac{L_2}{(t_2)} \right)^2 \right] \quad (5.18)$$

## Chapter 6

# The dynamics of Cl-Adamantane

A calorimetric study over Cl-Adamantane shows an anomalous heat-capacity hump around  $T = 310$  K, in the temperature range of plastically crystalline phase [1]. The temperature dependence of the anomalous heat capacities resembles somewhat a Schottky anomaly, which is an observed effect in solid state physics where the specific heat capacity has a peak, something anomalous because the heat capacity usually increases with temperature, or stays constant.

We believe that this calorimetric effect can be caused due to a change in the molecular reorientations dynamics of Cl-Adamantane, in its plastic phase. In order to study it, incoherent quasielastic neutron scattering experiments have been performed on 1-chloroadamantane at the corresponding temperature range.

### 6.1 Chloroadamantane

Chloro-adamantane  $C_{10}H_{15}Cl$ , formally known as 1-chloro-tricyclo[3,3,1,1] decane, is a rather huge cage-like molecule. It can be obtained from adamantane  $C_{10}H_{16}$  by substituting a chlorine atom for one hydrogen of a tertiary carbon. Assuming that this substitution does not change the rest of the molecule, the symmetry is  $C_{3v}$  [7].

Cl-adamantane presents an orientationally disordered phase, the so-called plastic phase, between 244 K, where it undergoes a first order transitions from an ordered monoclinic structure, and 442 K, where the plastic-liquid transition occurs. A material in a plastic phase, usually called plastic crystal, is characterized by weakly interactions between molecules that possess some orientational or conformational degrees of freedom. If the internal degree of freedom is molecular rotation, the name rotor phase or rotatory phase is also used, however, this rotation will not be completely free.

Studies [8, 6] about the Cl-adamantane plastic phase structure show the following features:

1. The lattice is face-centred cubic (FCC), with space group  $F_{m3m}$  and 4 molecules in the unit cell.
2. The molecules centre of mass are distributed along the lattice sites.
3. In one site, a molecule can occupy at least 24 equilibrium positions. These positions correspond to 6 orientations of the C-Cl chemical bond along the [100] directions. In each case the molecule has 4 possible equilibrium positions deducing themselves by a  $90^\circ$  rotation around the molecular axis.

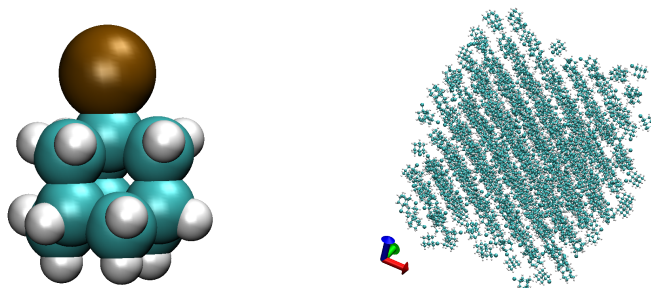


FIGURE 6.1: *Left)* Chloro-adamantane ( $C_{10}H_{15}Cl$ ) molecular structure, where carbons are in white, hydrogen in blue and the chlorine atom is in brown. *Right)* Molecular lattice in the plastic phase.

## 6.2 The QENS experiment

The IRIS spectrometer described in section 2.3 was used for performing the experiment, where the same sets of measurements were made to two different samples. The samples were prepared using a press to create a thin pellet layer from the Cl-adamantane powder, and two different thickness of about 0.55 and 0.3 millimeters were achieved. A vanadium flat can was used for holding the samples inside the spectrometer.

The energy of the neutrons incident on the sample is  $12.88 \text{ meV}$  ( $\lambda = 2.52 \text{ \AA}$ ) and the energy resolution is equal to  $17.5 \text{ } \mu\text{eV}$ . The experiment was performed through the detectors associated to the pyrolytic graphite crystal array. Thus, the measurements were made with 51 detectors which corresponds to a scattering angle  $\theta$  range from  $13.53^\circ$  to  $79.2^\circ$  and a momentum exchange  $Q$  range from  $0.442 \text{ \AA}^{-1}$  to  $1.854 \text{ \AA}^{-1}$ .

As the objective is to study the Cl-ADM plastic phase, measurements were made at 6 different temperatures belonging to that phase range, namely  $T = 260 \text{ K}$ ,  $280 \text{ K}$ ,  $300 \text{ K}$ ,  $320 \text{ K}$ ,  $340 \text{ K}$  and  $360 \text{ K}$ . The measurement for each temperature was done until the total neutron counts were the corresponding to  $300 \text{ } \mu\text{A}$ . Considering that the IRIS neutron current is about  $80 \text{ } \mu\text{A}/\text{hour}$ , each measurement lasts for about 4 hours.

For each measurement, IRIS detectors record the neutron time of flight spectra, which is called RAW data. Therefore the first thing to do is to convert this RAW data into the spectra  $S(Q, \omega)$  by the method explained in section 5.3.1. For doing that it has been used the Mantid's tool Indirect Data Reduction: Energy Transfer, which needs a file containing the most recent calibration information about the instrument.

Before being able to analyse the spectrum, it is necessary to subtract the background contribution due to the sample holder and the can. For getting this information, during the experiment it has also been measured an empty can.

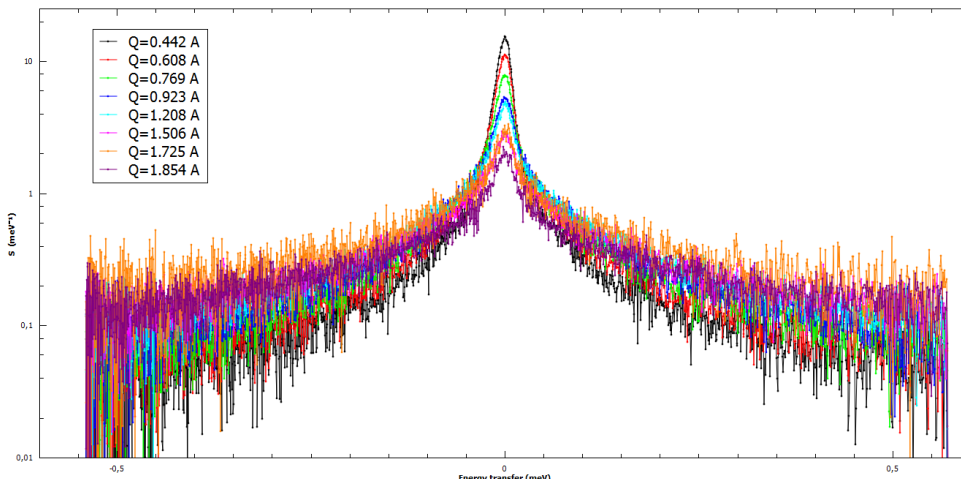


FIGURE 6.2: Spectrum  $S(Q, w)$ , for the measurement at 300 K, corresponding to detectors number 3, 7, 11, 15, 23, 33, 43 and 53 of the instrument, which correspond to  $Q$  values of  $0.442 \text{ \AA}^{-1}$ ,  $0.608 \text{ \AA}^{-1}$ ,  $0.769 \text{ \AA}^{-1}$ ,  $0.923 \text{ \AA}^{-1}$ ,  $1.208 \text{ \AA}^{-1}$ ,  $1.506 \text{ \AA}^{-1}$ ,  $1.725 \text{ \AA}^{-1}$  and  $1.854 \text{ \AA}^{-1}$  respectively.

For the following analysis, we are going to draw on the measurements results of the 0.3 mm thick sample. The reason is that with a thinner sample we reduce the multiple scattering effect. This effect is due to the fact that, if the sample is too wide, some neutrons may interact twice or more with the sample and it will affect to the measurement.

### 6.3 Analysis and discussion

The aim of the following analysis is to study the Cl-Adamantane molecular reorientations dynamics through the results of the quasielastic neutron scattering experiment performed over its plastic phase. For this purpose, as explained in chapter 5, it is necessary to analyse the incoherent scattering law, however, from the experiment we obtained the total  $S(Q, w)$ . As we know, the incoherent scattering law is included into the total one and, for an organic hydrogenated molecule such as Cl-Adamantane, the scattering becomes mainly incoherent. Therefore, all we need is a way to take the part we are interested in, and for that we are going to look to the  $S(Q)$  function, which comes from adding together all energies measured for each  $Q$  value.

In fig. 6.3 we can see two Bragg peaks around, approximately,  $1.1 \text{ \AA}^{-1}$  and  $1.25 \text{ \AA}^{-1}$ . These peaks appear due to the presence of a well-defined lattice in the Cl-Adamantane plastic phase because, as commented in section 6.1, the molecules center of mass remains in a FCC lattice sites. Hence, the incoherent scattering information related to the molecular dynamics will be in the spectra corresponding to  $Q$  values below  $1 \text{ \AA}^{-1}$  (where the first Bragg peak starts).

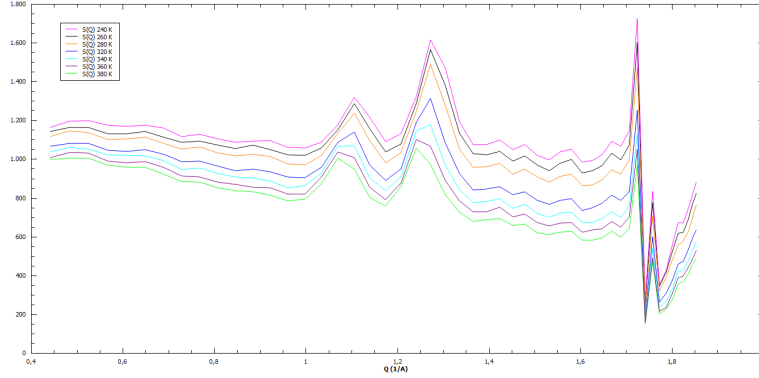


FIGURE 6.3: Scattering law  $S(Q)$  for all the temperatures measured.

Before tackling the fittings, there is still one thing remaining to do. It is necessary to use Mantid for carry out a rebinning to the data, both on energy ( $w$ ) and on momentum transfer ( $Q$ ). After that, we obtain new sets of data which maintain the same range in  $w$ , but with equally space data points and with less noisy information at the graph tails than what can be observed in fig. 6.2. With respect to  $Q$  we will obtain 7 different sets of data also equally spaced between  $0.45 \text{ \AA}^{-1}$  and  $1.05 \text{ \AA}^{-1}$ .

Firstly, we are going to try to discern how many dynamic processes underlie in the Cl-adamantane plastic phase. As we know from chapter 5, the incoherent scattering function  $S_{inc}(Q, w)$  in the elastic region consists in a purely elastic component,  $\delta(w)$ , and quasi-elastic components centered on  $w = 0$ , given by Lorentzian functions. We are going to perform model selection between 2 and 3 dynamic processes, therefore the mathematical expressions to use are:

$$S_{inc}(Q, w) = D \cdot \delta(w) + A \cdot \frac{\Gamma_1}{w^2 + (\Gamma_1)^2} + B \cdot \frac{\Gamma_2}{w^2 + (\Gamma_2)^2} \quad (6.1)$$

$$S_{inc}(Q, w) = D \cdot \delta(w) + A \cdot \frac{\Gamma_1}{w^2 + (\Gamma_1)^2} + B \cdot \frac{\Gamma_2}{w^2 + (\Gamma_2)^2} + C \cdot \frac{\Gamma_3}{w^2 + (\Gamma_3)^2} \quad (6.2)$$

where the Half-Width Half-Maximum parameter  $\Gamma_n$  is inversely proportional to a characteristic time  $\tau_n$  of the dynamic process  $n$ ,  $D$  is called the elastic structure factor and  $A$ ,  $B$  and  $C$  the quasielastic structure factors.

The analysis consists in performing Bayesian multi-fitting with respect to the Half-Width Half-Maximum parameters, for each temperature. In other words, we will fit, for each temperature separately, the 7 sets of data keeping the  $\Gamma$  parameters common for all of them, meanwhile the other parameters (the structure factors) will be free to vary for each set. Perhaps, it is also important to recall that the fitting function for the analysis is the convolution between the function described by the models and the resolution measured from the instrument.

Once all the fittings are performed, we take a look at the resulting fits and, apparently, the results for both models seems quite suitable to the experimental data.

However, if we draw upon the  $\chi^2$  Probability Density Function we realise how the hypothesis of considering only two dynamic processes is slightly better (see fig. 6.4).

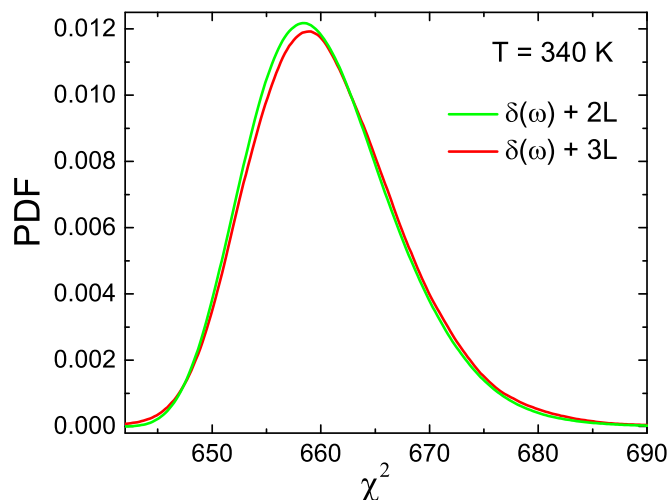


FIGURE 6.4:  $\chi^2$  Probability Density Function for the fitting with models defined by equations 6.2 ( $\delta(w)+3$  Lorentzian components) and 6.1 ( $\delta(w)+2$  Lorentzian components).

Fig. 6.5 shows the fit of the model corresponding to two QENS component (6.1) to a particular spectra of data ( $T = 340$  K and  $Q = 0.75 \text{ \AA}^{-1}$ ). There are also shown each component of the model disaggregated, in order to appreciate the contribution of each one two the total fit. It can be appreciate how the  $\delta(w)$  component takes exactly the shape of the resolution, something obvious due to the convolution of the model with the resolution.

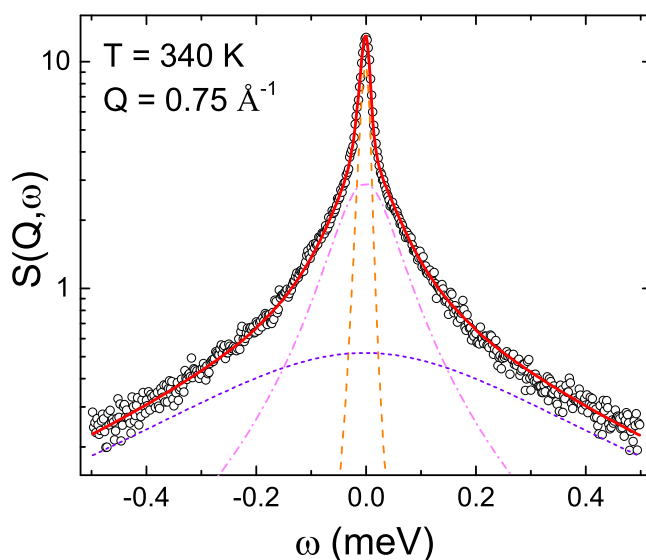


FIGURE 6.5: Resulting fit (red line) to the experimental data corresponding to  $T = 340$  K and  $Q = 0.75 \text{ \AA}^{-1}$ . Model components are also plotted disaggregated,  $\delta(w)$  with the orange dashed line and both Lorentzians with the purple dotted line and the pink dashed with points line.

Once it is determined how many dynamic processes underly the experimental results, we are going to take a look at the obtained results for the fitting parameters. Firstly, fig. 6.6 shows the evolution of the parameters  $\Gamma$  with the temperature.

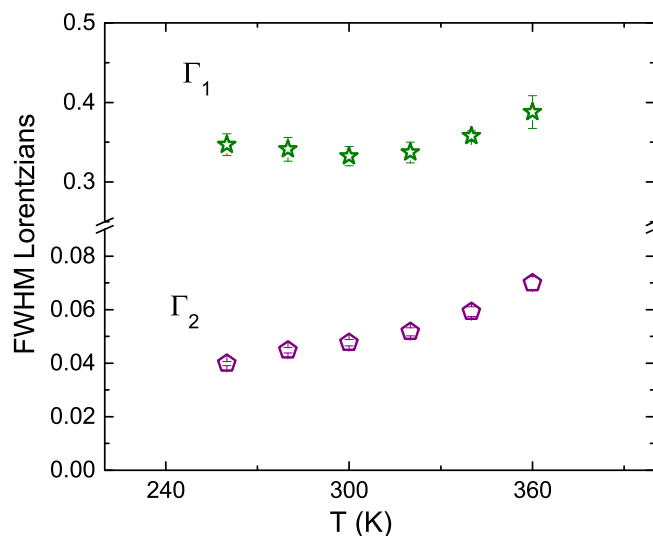


FIGURE 6.6: Plot of the resulting  $\Gamma$  parameters for the fitting with the model described by eq. 6.1 for all the temperatures measured.

The two  $\Gamma$  values differ by one order of magnitude and, as they are the inverse of characteristic times, we can make out that one of the processes is much faster than the other one. Fig. 6.6 also shows a slightly raise of  $\Gamma$  parameters with respect to the temperature increase. This means that temperature affects the molecular dynamics, which is really what we want to study.

Now, we are going to take a look to the structure factors results.

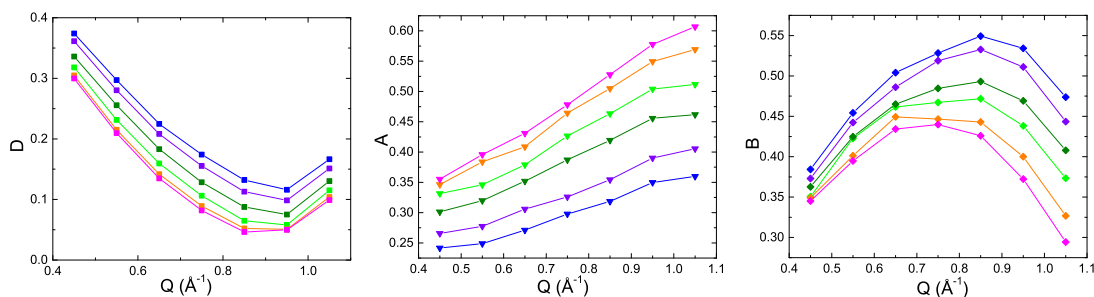


FIGURE 6.7: Structure factors  $D$  (left),  $A$  (middle) and  $B$  (right) resulting from the fittings for all temperatures, from 260 K (blue points) to 360 K (pink points). The lines are simply guides to the eye for better appreciate the evolution.

Fig. 6.7 shows different trends for each structure factor and how these trends remain the same for all temperatures. The value of these factors stands out the relevance of each component of the model to the total fit, and as they change according to  $Q$ , it

means that each component has different weight depending on  $Q$ . Parameter  $D$  (factor for component  $\delta(w)$ ) decays with increasing  $Q$ , just the opposite of parameter  $A$  (factor for one Lorentzian component). Meanwhile, parameter  $B$  (factor for the other Lorentzian component) starts increasing and finishes falling, an effect that is more pronounced for higher temperatures. We can also notice that for  $Q$  values close enough to 0, the elastic component  $\delta(w)$  is going to be the most relevant while the quasielastic ones become negligible, as would be expected [16].

Finally, Cl-Adamantane molecule can be considered oblong shaped, which means it has one dimension considerably larger than the other two. Hence, we can try a model which describes the molecular dynamics physically based on this geometric feature of the molecule. In fact, certain studies [20] provides analysis for rotational correlation functions of single molecules that suits the hypothesis of an oblong molecule rotation. Following their development, applied to incoherent neutron scattering analysis, it is assumed that rotational diffusion coefficients  $D_x$  and  $D_y$  are equal, but different from  $D_z$ , it is obtained the following model:

$$S_{inc}(Q, w) = \sum_{l=0}^{\infty} A_l \cdot \sum_{m=-l}^l \frac{\Gamma_l^m}{w^2 + (\Gamma_l^m)^2} \quad (6.3)$$

with a Half-Width Half-Maximum parameter  $\Gamma_l^m$  given by:

$$\Gamma_l^m = l(l+1)D_x + m^2(D_z - D_x) \quad (6.4)$$

We are not going to deal with the analytical expression of coefficient  $A_l$  and we will consider it as a fitting parameter. Otherwise, the model can be understood as a collection of Lorentzians with variable widths and. The summation over all  $l$  values will be truncated at  $l = 2$  for the fitting, so that we obtain the final expression:

$$\begin{aligned} S_{inc}(Q, w) = & A_0 \cdot \delta(w) + A_1 \left[ 2 \frac{D_x + D_z}{w^2 + (D_x + D_z)^2} + \frac{2D_x}{w^2 + (2D_x)^2} \right] \\ & + A_2 \left[ 2 \frac{2D_x + 4D_z}{w^2 + (2D_x + 4D_z)^2} + 2 \frac{5D_x + D_z}{w^2 + (5D_x + D_z)^2} + \frac{6D_x}{w^2 + (6D_x)^2} \right] \end{aligned} \quad (6.5)$$

We carry out the fitting of all the experimental data with the previous model, in the same way that the one explained for fitting with expressions 6.1 and 6.2. Fig. 6.8 shows the fits to certain representative spectra for all the temperatures measured.

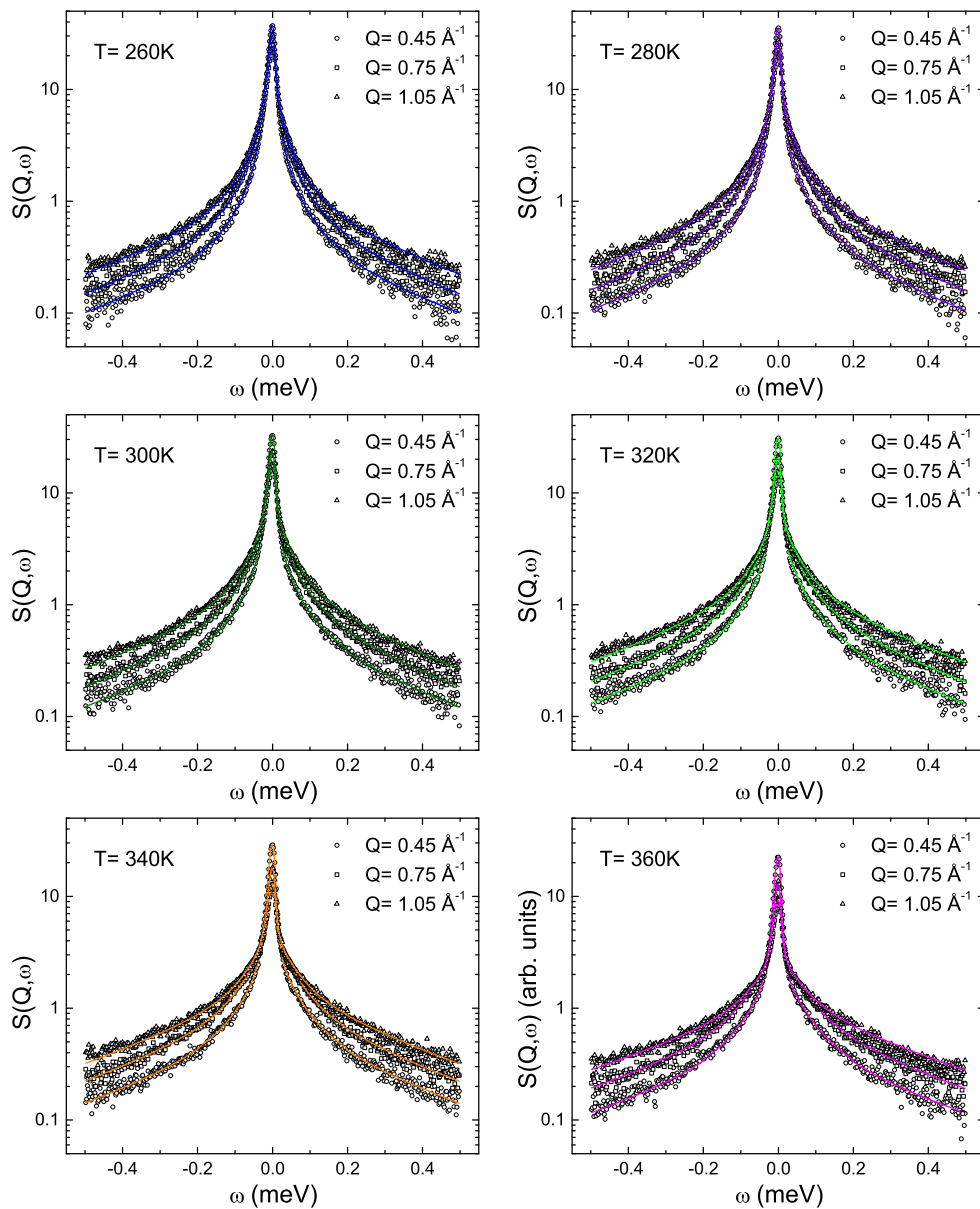


FIGURE 6.8: Fits to the experimental data by the model defined by eq. 6.5. For each temperature there are shown the spectra corresponding to  $Q = 0.45, 0.75$  and  $1.05 \text{ \AA}^{-1}$ .

The model used provides directly the rotational diffusion coefficients  $D_x$  and  $D_z$ , which units are  $\frac{\text{rad}^2}{\text{s}}$  and which results are shown in fig. 6.9.

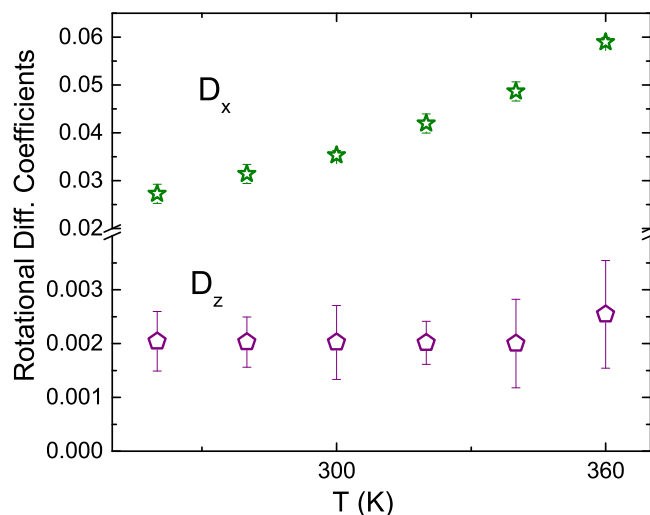


FIGURE 6.9: Plot of the resulting  $\Gamma$  parameters with the model described by eq. 6.5 for all the temperatures measured.

The rotational diffusion coefficients values obtained differ about one order of magnitude, what means that the rotational diffusion around  $x$  axis is much faster than around  $z$  axis. Another feature that can be concluded from fig. 6.9 is that rotational diffusion around  $x$  axis increases proportionally with the temperature. However, rotational diffusion around  $z$  axis seems not to be affected by temperature, at least until temperature reaches the highest values, when it is appreciated a slightly increment in the  $D_z$  rotational diffusion coefficient. In fact, this phenomenon is better appreciated if we look at the degree of anisotropy  $\delta$  which gives the quotient between the two rotational diffusion coefficients,  $\delta = \frac{D_z}{D_x}$ . Fig. 6.10 shows clearly how the anisotropy of the molecular movement changes at temperatures around 340 K.

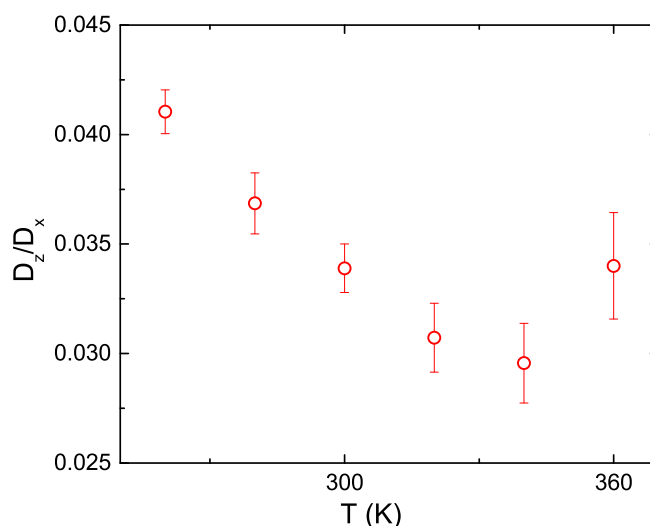


FIGURE 6.10: Degree of anisotropy  $\delta = \frac{D_z}{D_x}$  for all the temperatures measured.

## 6.4 Conclusions

Bayesian analysis of the experimental data has been used to prove how many dynamic processes better describe the results obtained from the quasielastic neutron scattering experiment performed on Cl-adamante, in its plastic phase temperature range. The model selection through  $\chi^2$  PDFs concludes that 2 processes are a better hypothesis than 3, something that could not have been concluded by a frequentist approach.

A fitting which a model, which consider the Cl-adamante as an oblong shaped molecule, has allow to calculate the rotational diffusion coefficients  $D_x$  and  $D_z$ . This analysis also allows to conclude that while the rotation around  $x$  axis increases proportionally with the temperature, the rotational diffusion around  $z$  does not behave in the same way. It remains constant for the lower temperatures measured, but it seems to increase for temperatures higher than 340 K. An effect that is appreciated much better when looking at the degree of anisotropy in function of the temperature. This phenomenon could be related with the anomalous calorimetric effect introduced at the beginning of the chapter. Perhaps, the atypical evolution of the heat-capacity at temperatures around 310 K, could be related with the observed rotational diffusion activation around  $z$  axes at similar temperatures.

Probably, it is necessary a deeper analysis in order to indeed understand the molecular dynamics occurring in the Cl-Adamantane plastic phase at the range of temperatures of interest. It would also be necessary to define a more rigorous explanation for the relation between the dynamic evolution found and the unexplained calorimetric effect. Nevertheless, we have set the way that the oblong molecule hypothesis is a good approach and that has been possible due to performing an accurate Bayesian analysis.

# Bibliography

- [1] K. Kobashi, T. Kyomen and M. Oguni *J. Phys. Chem. Solids* Vol. 59, No. 5, pp. 667-677 (1998).
- [2] L. C. Pardo, M. Rovira-Esteva, S. Busch, J. F. Moulin and J. Ll. Tamarit *Phys. Rev. E* **84** 046711 (2011).
- [3] L. C. Pardo, M. Rovira-Esteva, S. Busch, M. D. Ruiz-Martín J. Ll. Tamarit and T. Unruh *e-print arXiv:0907.3711* (2009).
- [4] L. C. Pardo, M. Rovira-Esteva, S. Busch, M. D. Ruiz-Martín and J. Ll. Tamarit *J. Phys.: Conf. Ser.* **325** 012006 (2011).
- [5] D. Monserrat, A. Vispa, L. C. Pardo, R. Tolchenov, S. Mukhopadhyay and F. Fernández-Alonso *J. Phys.: Conf. Ser.* **663** 012009 (2015).
- [6] J. P. Amoureux, M. Bée and J. L. Sauvajol *Molecular Physics* **45**, 709-719 (1982).
- [7] M. Bée and J. P. Amoureux *Molecular Physics* Vol. 48, No. 1, 63-79 (1983).
- [8] M. Foulon, T. Belgrand, C. Gors and M. More *Acta Cryst.* **B45**, 404-411 (1989).
- [9] D. S. Sivia and J. Skilling, *Data Analysis: A Bayesian Tutorial* (Oxford University Press, New York, 2006).
- [10] T. Bayes *Phil. trans. Roy. Soc. London* 53 370 (1764).
- [11] N. Metropolis, A. Rosenbluth, M. Rosenbluth, A. Teller, and E. Teller, *J. Chem. Phys.* **21**, 1087 (1953) .
- [12] The latest version of the MANTID software package can be downloaded free of charge from <http://download.mantidproject.org/>
- [13] D. S. Sivia and C. J. Carlile *J. Chem. Phys.* **96** 170-178 (1992).
- [14] M. Bée, *Quasielastic Neutron Scattering: Principles and Applications in Solid State Chemistry, Biology and Materials Science* (Adam Hilger, Bristol and Philadelphia, 1988).
- [15] G. L. Squires, *Introduction to the Theory of Thermal Neutron Scattering* (Cambridge University Press, Cambridge, 1978).
- [16] B. T. M. Willis and C. J. Carlile, *Experimental Neutron Scattering*, (Oxford University Press, Oxford, 2009).
- [17] V. F. Sears *Can. J. Phys.* Vol. **44** (1966).

- [18] S. Mukhopadhyay 2014 *Rutherford Appleton Laboratory Technical Report RAL-TR-2014-005* (Didcot, UK, 2014).
- [19] V. García-Sakai, M. A. Adams, W. S. Howells, M. T. F. Telling, F. Demmel and F. Fernández-Alonso *Rutherford Appleton Laboratory Technical Report RAL-TR-2011-004* (Didcot, UK, 2011).
- [20] G. Hinze, G. Diezemann, and T. Basché *Phys. Rev. Lett.* **93**, 203001 (2004).